

1 *Research article*

2 **Automated riverbed composition analysis using Deep Learning** 3 **on underwater images**

4 Alexander A. Ermilov¹, Gergely Benkő¹ and Sándor Baranya¹

5 ¹Department of Hydraulic and Water Resources Engineering, Budapest University of Technology and Economics,
6 Budapest, 1111, Hungary

7 *Correspondence to:* Alexander A. Ermilov (ermilov.alexander@emk.bme.hu)

8 **Abstract.** The sediment of alluvial riverbeds plays a significant role in river systems both in engineering and
9 natural processes. However, the sediment composition can show great spatial and temporal heterogeneity, even
10 on river reach scale, making it difficult to representatively sample and assess. Conventional sampling methods in
11 such cases cannot describe well the variability of the bed surface texture due to the amount of energy and time
12 they would require. In this manuscript, an attempt is made to overcome this issue by introducing a novel image-
13 based, Deep Learning (DL) algorithm and related field measurement methodology with potential for becoming a
14 complementary technique for bed material samplings and significantly reducing the necessary resources. The
15 algorithm was trained to recognise main sediment classes in videos that were taken underwater in a large river
16 with mixed bed sediments, along cross-sections, using In total, 27 physical bedmaterial samples were collected
17 and sieved for the validation purposes. The introduced DL-based method is fast, i.e., the videos of 300-400-meter-
18 long sections can be analysed within minutes, with very dense spatial sampling distribution. The goodness of the
19 trained algorithm was evaluated i) mathematically by dividing the annotated images into test and validation sets,
20 and also via ii) intercomparison with other direct (sieving of physical samples) and indirect sampling methods
21 (wavelet-based image processing of the riverbed images), focusing on the percentages of the detected sediment
22 fractions. For the final evaluation, the sieving analysis of the collected physical samples were considered as the
23 ground truth. This meant a total of 27 measurement points, where the DL-results could be compared with the two
24 other methods. During data processing, outlier points, where the collected physical samples did not represent the
25 riverbed surface images taken there (e.g., due to bedarmour), were removed. In the remaining 14 points, the DL
26 algorithm produced promising results with a mean error of 4.5%. Besides, the spatial trend in the fraction changes
27 was also well captured along the cross-sections, based upon the visual evaluation of the footages. Furthermore,
28 comparison with the wavelet-based image processing justified the selection of the outlier points earlier, as its
29 results matched closely with the DL detections in these purely gravel-covered points and showed no sign of finer
30 fractions, univocally opposing the content of the physical samples. Suggestions for performing proper field
31 measurements are also given, furthermore, possibilities for combining the algorithm with other techniques are
32 highlighted, briefly showcasing the multi-purpose of underwater videos for hydromorphological assessment.

33 **Keywords:** riverbed texture, underwater mapping, sediment classes, Artificial Intelligence, Deep Learning,
34 image-based

35 **1 Introduction**

36 The physical composition of a riverbed plays a crucial role in fluvial hydromorphological processes, as a sort of
37 boundary condition in the interaction mechanisms between the flow and the solid bed. Within these processes, the

38 grains on the riverbed are responsible for multiple phenomena, such as flow resistance (Vanoni and Hwang, 1967;
39 Zhou et al., 2021), stability of the riverbed (Staudt et al., 2018; Obodovskyi et al., 2020), development of bed
40 armour (Rákóczi, 1987; Ferdowsi et al., 2017), sediment clogging (Rákóczi, 1997; Fetzer et al., 2017), fish shelter
41 (Scheder et al., 2015), etc. Through these physical processes, the bed material composition has a determining
42 effect on numerous river-uses, e.g., possibilities of inland waterway transport (Xiao et al., 2021), drinking water
43 supply through bank filtration (Cui et al., 2021), or the quality of riverine habitats (Muñoz-Mas et al., 2019)..
44 Knowledge of riverbed morphology and sediment composition (sand, gravel and cobble content) is therefore of
45 major importance in river hydromorphology. In order to gain information about riverbed sediments, in situ field
46 sampling methodologies are implemented.

47

48 Traditionally, bed material sampling methods are intrusive (i.e., sediment is physically extracted from the bed for
49 follow-up analysis) and carried out via collecting the sediment grains one-by-one (areal, grid-by-number and
50 pebble count methods, see e.g., Bunte and Abt, 2001; Guerit et al., 2018) or in a larger amount by a variety of
51 grab samplers (volumetric methods, such as WMO, 1981; Singer, 2008). This is then followed by measuring their
52 sizes individually on-site or transporting them to a laboratory for mass-sieving analysis (Fehr, 1987; Diplas, 1988;
53 Bunte and Abt, 2001). These sampling procedures are time- and energy consuming, especially in large gravel and
54 mixed bed rivers, where characteristic grain sizes can strongly vary both in time and space (Wolcott and Church,
55 1991; USDA, 2007), requiring a dense sampling point allocation. The same goes for critical river reaches, where
56 significant human impact led to severe changes in the morphological state of the rivers (e.g., the Upper section of
57 the Hungarian Danube; Török and Baranya, 2017). When assessing bed material composition on a river reach
58 scale, experts usually try to extrapolate from the samples, and describe larger regions of the bed (even several
59 thousand m²) by data gathered in a few, several dozen points (see e.g., USDA, 2007; Haddadchi et al., 2018;
60 Baranya et al., 2018; Sun et al., 2021). Gaining a representative amount of the sediment samples is also a critical
61 issue. For instance, following statistical criteria such as those of Kellerhals and Bray (1971) or Adams (1979), a
62 representative sample should weigh ten-to-hundred kg. Additionally, physical bed material sampling methods are
63 unable to directly quantify important, hydromorphological features such as roughness or bedforms (Graham et al.,
64 2005). Due to these constraints, surrogate approaches have recently been intensively tested to analyse the riverbed.
65 Major examples are introduced in the rest of this section. Unlike the conventional methods, these techniques are
66 non-intrusive and rely on computers and other instrumentation to decrease the need of human intervention and
67 speed up the analyses.

68

69 One group of the surrogate approaches is the acoustic methods, where an acoustic wave source (e.g., an Acoustic
70 Doppler Current Profiler; ADCP) is pointed towards the riverbed from a moving vessel, emitting a signal. The
71 strength and frequency of this signal is measured while it passes through the water column, reflecting back to the
72 receiver from the sediment transported by the river, and finally from the riverbed itself. This approach is fast and
73 larger areas can be covered relatively quickly (Grams et al., 2013). While it has already become widely used for
74 describing sediment movement (i.e., suspended sediment, Guerrero et al., 2016; bedload, Muste et al., 2016; and
75 indirectly flow velocity; Shields and Rigby, 2005) and channel shape (Zhang et al., 2008), it has not reached
76 similar breakthrough for riverbed material analysis. Researchers experimented with the reflecting signal strength
77 [dB] from the riverbed (e.g., Shields, 2010) to establish its relationship with the riverbed material. Their hypothesis

78 was that the absorption (and hence the reflectance) of the acoustic waves reaching the bed correlates with the type
79 of bed sediment. Following initial successes, the method presented several disadvantages and limitations, hence
80 it could not establish itself as surrogate method for riverbed material measurements so far. For example, Shields
81 (2010) showed that it was necessary to apply instrument specific coefficients to convert the signal strength into
82 bed hardness, and these coefficients could only be derived by first validating each instrument using collected
83 sediment samples with corresponding ADCP data. Moreover, the method was sensitive to the bulk density of the
84 sediment and to bedforms. Based on his results and observations, the sediment classification could only extend to
85 differentiate between cohesive (clay, silt) and non-cohesive (sand, gravel) sediment patches, but gravel could not
86 be distinguished strongly from sand as they produced similar backscatter strengths. Buscombe et al. (2014a;
87 2014b) further elaborated on the topic and successfully developed a better, less limited, decision tree-based
88 approach. They showed that spectral analysis of the backscatter is much more effective for differentiating the
89 sediment types compared to the statistical analysis used by Shields. With this approach it became possible to
90 classify homogenous sand, gravel, and cobble patches. However, Buscombe et al. (2014a, 2014b) also emphasizes
91 that acoustic approaches are not capable of separating the effects of surface roughness from the effects of
92 bedforms, therefore the selection of an appropriate ensemble averaging window size is of great importance for
93 their introduced method. This size has to be small enough to not include morphological signal, for which however,
94 the a priori analyses of riverbed elevation profiles is needed at each site. Furthermore, they suggest their method
95 is sensitive to and limited by high concentrations of (especially cohesive) sediment, therefore its application to
96 heterogeneous riverbeds would require site specific calibrations. The above-mentioned studies also note that
97 acoustic methods in general inherently do not allow the measurement of individual sediment grains due to their
98 spatial averaging nature. The detected signal strength correlates with the median grainsize of the covered area,
99 information about other nominal grain sizes cannot be gained.

100

101 Another group of the surrogate approaches is the application of photography (Adams, 1979; Ibbekken and
102 Schleyer, 1986) and later computer vision or image-processing techniques. During the last two decades, two major
103 subgroups emerged: one uses object- and edge detection (by finding abrupt changes in intensity and brightness of
104 the image, segmenting objects from each other; Sime and Ferguson, 2003; Detert and Weitbrecht, 2013), and the
105 other one analyses the textural properties of the whole image, using autocorrelation and semi-variance methods
106 to define empirical relationship between image texture and the grain sizes of the photographed sediments (Rubin,
107 2004; Verdú et al., 2005). Both image processing approaches were very time consuming and required mostly site-
108 specific manual settings, however, a few transferable and more automated techniques have also been developed
109 recently (e.g., Graham et al., 2005; Buscombe, 2013). Even though there is a continuous improvement in the
110 applied image-based bed sediment analysis methods, there are still major limitations the users face with, such as:

111

- 112 • Most of the studies (all the ones listed above) focuses on gravel bed rivers, and only a few exceptions
113 can be found in the literature where sand is also accounted for (texture-based methods; e.g.:
114 Buscombe, 2013).
- 115 • The adaptation environment was typically non-submerged sediment, instead of underwater
116 conditions (a few exceptions: Chezar and Rubin, 2004; Warrick et al., 2009).

- 117 • The computational demand of the image processing is high (e.g., one to ten minutes per image;
118 Detert and Weitbrecht, 2013).
- 119 • The analysis requires operator expertise (higher than in case of any conventional method).
- 120 • There is an inherent pixel- and image resolution limit (Buscombe and Masselink, 2008 Cheng, 2015;
121 Purinton and Bookhagen, 2019). The finer the sediment, the higher resolution of the images is
122 required (higher calculation time), or they must be taken from a closer position (smaller area and
123 sample per image).

124

125 Nowadays, with the rising popularity of Artificial Intelligence (AI), several Machine Learning (ML) techniques
126 have been implemented in image recognition as well. The main approaches of segmentation contra textural
127 analysis still remain; however, an AI defines the empirical relationship between the object sizes (Ighatinatane et
128 al., 2009; Kim et al., 2020) or texture types (Buscombe and Ritchie, 2018) in the images and their real sizes. In
129 the field of river sedimentology a few examples can already be found, where ML (e.g., Deep Learning; DL) was
130 implemented. For instance, Rozniak et al. (2019) developed an algorithm for gravel-bed rivers, performing
131 textural analysis. With this approach, information is not gained on individual grains (e.g., their individual shape
132 and position), but rather the general grain size distribution (GSD) of the whole images. At certain points of the
133 studied river basins, conventional physical samplings (pebble count) were performed to provide real GSD
134 information. Using this data, the algorithm was trained (with ~1000 images) to estimate GSD for the rest of the
135 study site, based on the images. The method worked for areas where grain diameters were larger than 5 mm, and
136 the sediment was well-sorted. The developed method showed sensitivity to sand coverage, blurs, reduced
137 illuminations (e.g., shadows) and white pixels. Soloy et al. (2020) presented an algorithm which used object
138 detection on gravel- and cobble covered beaches to calculate individual grain sizes and shapes. 46 images were
139 used for the model training, however, the number of images were multiplied with data augmentation (rotating,
140 cropping, blurring the images; see Perez and Wang, 2017) to enhance the learning session and increase the input
141 data. The method was able to reach a limited execution speed of a few seconds per m² and adequately measured
142 the sizes of gravels. Ren et al. (2020) applied an ensemble bagging-based Machine Learning (ML) algorithm to
143 estimate GSD along the 70 km long Hanford Reach of the Columbia River. Due to its economic importance, a
144 large amount of measurement data has been accumulated for this study site over the years, making it ideal for
145 using ML. By the time of the study, 13,372 scaled images (i.e., their millimetre/pixel ratio was known) were taken
146 both underwater and in the dry zones, covering approx. 1 m² area each. The distance between the image-sampling
147 points was generally between 50-70 m. An expert defined the GSD (8 sediment classes) of each image by using a
148 special, visual evaluation-classification methodology (DeLong and Brusven, 1991; Geist et al., 2000). This dataset
149 was fed to a ML algorithm along with their corresponding bathymetric attributes and hydrodynamic properties,
150 simulated with a 2D hydrodynamic model. Then, it was tested to predict the sediment classes based on the
151 hydrodynamic parameters only. The algorithm performed with a mean accuracy of 53%. Even though this method
152 was not image-based (only indirectly, via the origin of the GSD data), it highlighted the possibilities of an AI for
153 a predictive model, using a high-dimensional dataset. Having such a large data of grain size information can be
154 considered exceptional and takes a huge amount of time to gather, even with the visual classification approach
155 they adapted. Moreover, this was still considered spatially sparse information (point-like measurements, 1 m²
156 covered area/image dozens of meters away from each other). Buscombe (2020) used a set of 400 scaled images

157 to train an AI algorithm on image texture properties, using another image-processing method (Barnard et al., 2007)
158 for validation. The algorithm reached a good result for not only gravel, but sand GSD calculation as well,
159 outperforming an earlier, but promising, texture-based method (wavelet analysis; Buscombe, 2013). In addition,
160 the method required fewer calibration parameters than the wavelet image-processing approach. The study also
161 foresaw the possibility to train an AI which estimates the real sizes of the grains, without knowing the scale of
162 one pixel (mm/pixel ratio) if the training is done properly. The AI might learn unknown relationships between the
163 texture and sizes if it is provided with a wide variety (images of several sediment classes) and scale (mm/pixel
164 ratio)) of dataset (however, it is also prone to learn unwanted biases). Recently, Takechi et al. (2021) further
165 elaborated on the importance of shadow- detection and removal, using a dataset of 500 pictures for training a
166 texture-based AI, with the help of an object-detecting image-processing technique (Basegrain; Detert and
167 Weitbrecht, 2013). The previously presented studies, applying ML and DL techniques, significantly contributed
168 to the development and improvement of surrogate sampling methods, incorporating the great potential in AI.
169 However, there are still several shortcomings to these procedures. Firstly, none of the image-based AI studies
170 used underwater recordings, even though the underwater environment offers completely different challenges.
171 Secondly, the training images were always scaled, i.e., the sizes of the grains could be easily reconstructed, which
172 is again complicated to accomplish in a river. Lastly, they were not adapted for continuous (i.e., spatially dense)
173 measurement, but rather focused on a sparse grid-like approach.

174

175 The goal of this manuscript is to further investigate the applicability of image processing as a surrogate method,
176 and attempt to break through or go around the above mentioned shortcomings of the AI-based approaches. Hence,
177 we introduce a riverbed material analysing, Deep Learning (DL) algorithm and field measurement methodology,
178 along with our first set of results. The introduced technique can be used to measure the gravel and sand content of
179 the submerged riverbed surface. It aims to eventually become a practical tool for exploratory mapping, by
180 detecting sedimentation features (e.g., deposition zones of fine sediment, colmation zones, bed armour) and
181 helping decision making for river sedimentation management. Also, the long-term hypothesis of the authors
182 includes the creation of an image-based measurement methodology, where underwater videos of the riverbed
183 could serve multiple sediment related purposes simultaneously. Part of which is the current approach for mapping
184 the riverbed material texture and composition. Others include measuring the surface roughness of the bed (Ermilov
185 et al., 2020) and detecting bedload movement (Ermilov et al., 2022).

186

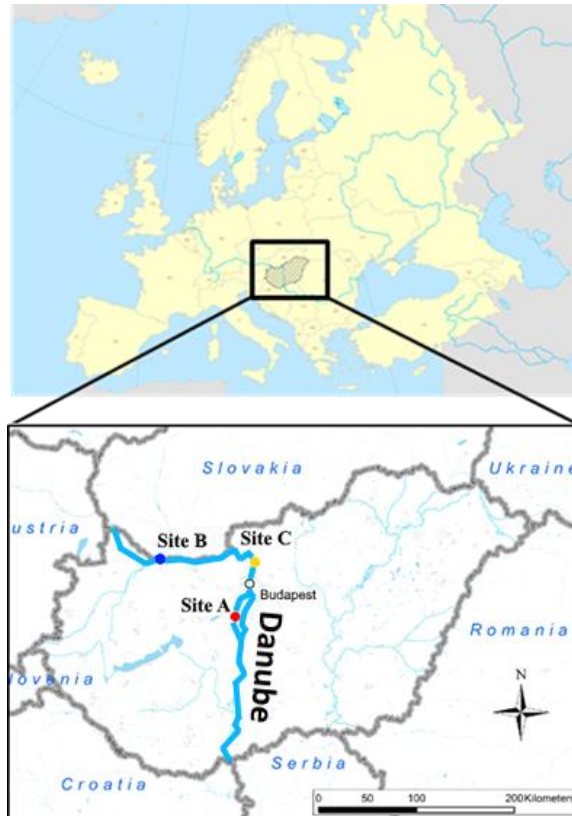
187 Compared to the studies introduced earlier, the main novelty of our manuscript is that both the training and
188 analysed videos are recorded underwater, continuously along cross-sections of a large river. Furthermore, the
189 training is unscaled, i.e., the camera-riverbed distance could vary while recording the videos, without considering
190 image-scale. Moreover, compared to the relatively low number of training images in most of the above referred
191 studies, we used a very large dataset (~15000) of sediment images for the texture-based AI, containing mostly
192 sand, gravel, cobble, and to a smaller extent: bedrock together with some other, non-sediment related objects.

193

194 **2 Methods**

195 **2.1 Case studies**

196 The results presented in this study are based on riverbed videos taken during three measurement campaigns, in
197 sections of the Danube River, Hungary. The first campaign was at Site A, Ercsi settlement (~ 1606 rkm) where 3
198 transects were recorded, the second one was at Site B, Gönyű settlement (~ 1791 rkm) with 2 transects, and the
199 third was at Site C, near to Göd settlement (~ 1667 rkm) with 2 transects (Fig. 1). Each transect was recorded
200 separately (one video per transect), therefore our dataset included a total of 8 videos.



201 **Figure 1: The location of the riverbed videos, where the underwater recordings took place. All sites were located in**
202 **Hungary, Central Europe. The surveys were carried out on the Danube River, Hungary’s largest river.**
203

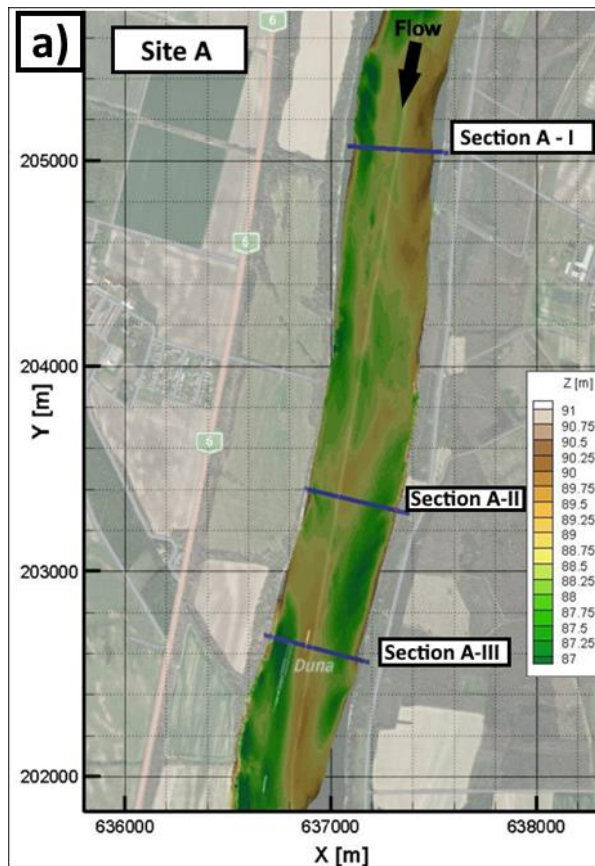
204 The training of the DL algorithm was done using the video images of Site C and a portion of A (test set; see later
205 in Section 2.3), while Site B and the rest of the images from A served for validation. The measurements were
206 carried out during daytime, at mid-water regime ($Q = 1900 \text{ m}^3/\text{s}$) in case of Site A, and low water regime ($Q =$
207 $1350 \text{ m}^3/\text{s}$) at Site B, and Site C ($Q = 700 \text{ m}^3/\text{s}$). This latter site served only for increasing the training image
208 dataset (i.e., conventional samplings were not carried out at the time of recording the videos), thus we do not go
209 into further details with it for the rest of the manuscript, but the main characteristics are listed in Table 1.

210

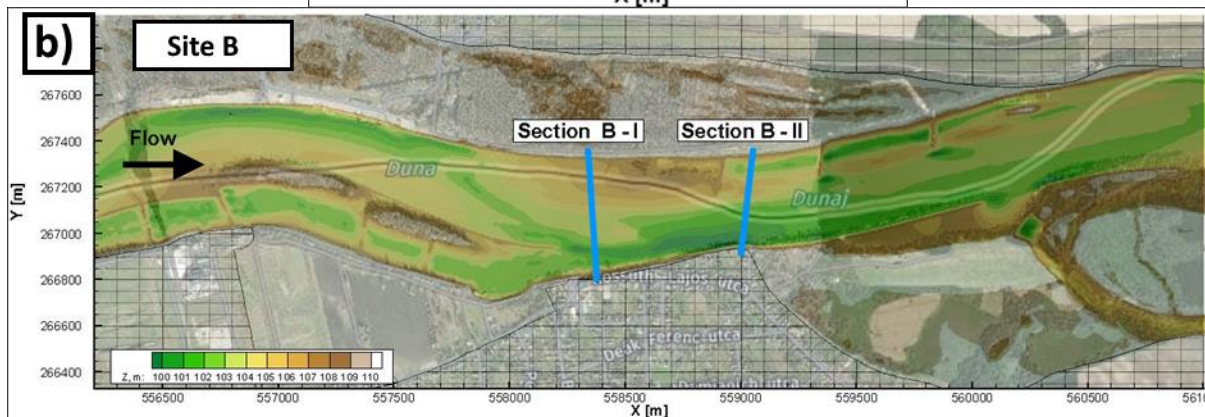
	Site A	Site B	Site C
Q_{survey} [m^3/s]	1900	1350	700
B_{survey} [m]	300 – 450		
$H_{\text{mean, survey}}$ [m]	3.5 - 4.5		
S_{survey} [cm/km]	15		
SSC_{survey} [mg/l]	25	20	14
Characteristic sediment riverbed	gravel, sandy gravel	gravel, gravelly sand	gravel, sandy gravel
$Q_{\text{annual, mean}}$ [m^3/s]	2000	2200	1400
$Q_{1\%}$ [m^3/s]	5300	5500	4700

211 **Table 1: Main hydromorphological parameters of the measurement sites. Q_{survey} : discharge during survey; B_{survey} : river**
212 **width during survey; $H_{\text{mean, survey}}$: mean water depth during the survey; S_{survey} : riverbed slope during survey; SSC_{survey} :**
213 **mean suspended sediment concentration during the survey; $Q_{\text{annual, mean}}$: annual-mean of the discharge at the site; $Q_{1\%}$:**
214 **flood with 1% annual exceedance probability.**

215 As underwater visibility conditions are influenced by the suspended sediment (SSC_{survey} – susp. sed.
216 concentration), the characteristics of this sediment transport is also included in Table 1. The highest water depths
217 were around 6-7 m in all cases. In Site A, measurements included mapping of the riverbed with a camera along
218 three separate transects (Fig. 2a). At Site B, two transects were recorded (Fig. 2b).



219



220

221

222

223

224

Figure 2: Bathymetry of Site A and B The measurement cross-sections are also marked. The vessel moved along these lines from one bank to the other, while carrying out ADCP measurement and recording riverbed videos. Physical bed material samples were also collected in certain points of these sections. The X and Y coordinates are given in EOVS, which refers to the Hungarian Uniform National Projection system,

225

226 2.2 Field data collection

227

228

229

230

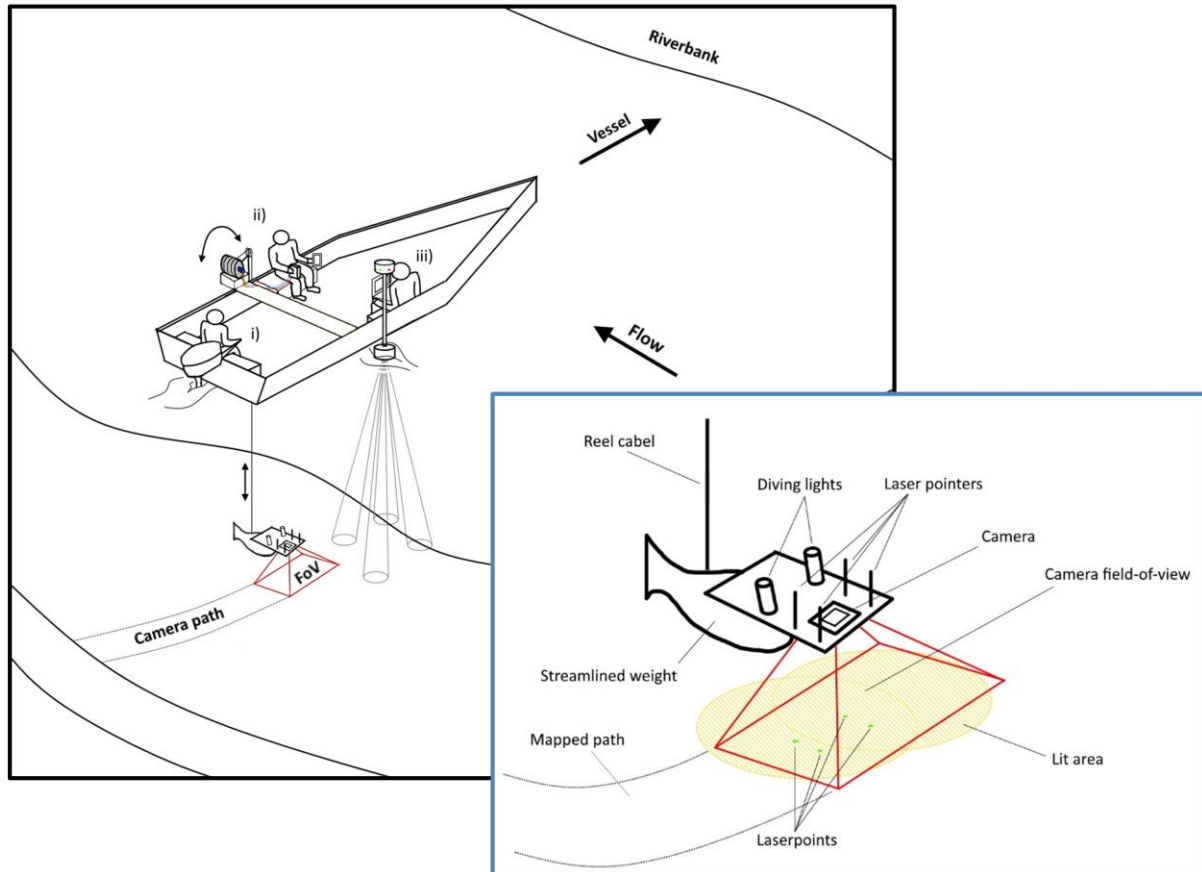
231

232

233

Fig. 3 presents a sketch of the measurement process with the equipment and a close-up of the underwater instrumentation. During the field measurements, the camera was attached to a streamlined weight (originally used as an isokinetic suspended sediment sampler) and lowered into the water from the vessel by an electric reel. The camera was positioned perpendicularly to the water and the riverbed, in front of the nose of the weight. Next to the camera, two diving lights worked as underwater light sources, focusing into the camera's field of view (FoV). In addition, four laser pointers were also equipped in hand-made isolation cases to provide possible scales for secondary measurements. They were also perpendicular to the bottom, projecting their points onto the underwater

234 camera field of view. Their purpose was to ensure a visible scale (mm/pixel ratio) in the video footages for
235 validation. During the measurement procedure, a vessel crossed the river slowly through river transects, while the
236 position of the above detailed equipment was constantly adjusted by the reel. Simultaneously, ADCP and RTK
237 GPS measurement were carried out by the same vessel, providing water depth, riverbed geometry, flow velocity,
238 ship velocity and position data. Based on this information and by constantly checking the camera's live footage
239 on deck, the camera was lowered or lifted to keep the bed in camera sight and avoid colliding with it. The sufficient
240 camera – riverbed distance depended on the suspended sediment concentration near the bed and the used
241 illumination. The reel was equipped with a register, with its zero adjusted to the water surface. This register was
242 showing the length of cable already released under the water, effectively the rough distance between the water
243 surface and the camera (i.e., the end of the cable). Of course, due to the drag force this distance was not vertical,
244 but this value could be continuously compared to the water depth measured by the ADCP. Differencing these two
245 values, an approximation for the camera – riverbed distance was given all time. The sufficient difference could
246 be established by monitoring the camera footage while lowering the device towards the bed. This value was then
247 to be maintained with smaller corrections during the survey of the given cross-section, always supported by
248 observing the camera recording, and adjusting to environmental changes. The vessel's speed was also adjusted
249 based on the video and slowed down if the video was blurry or the camera got too far away from the bed (see later
250 in Section 3.3). The measurements required three personnel to i) drive the vessel, ii) handle the reel, adjust the
251 equipment position, and monitor the camera footage, iii) monitor the ADCP data, while communicating with the
252 other personnel (see Fig. 3).



253
 254 **Figure 3: Left: sketch of the measurement process. The vessel was moving perpendicular to the riverbank along a cross-**
 255 **section (i). A reel was used to lower a camera close to the riverbed (ii). Simultaneously, the bed topography and water**
 256 **depth were measured by an ADCP (iii). Right: Close-up sketch of the underwater instrumentation.**

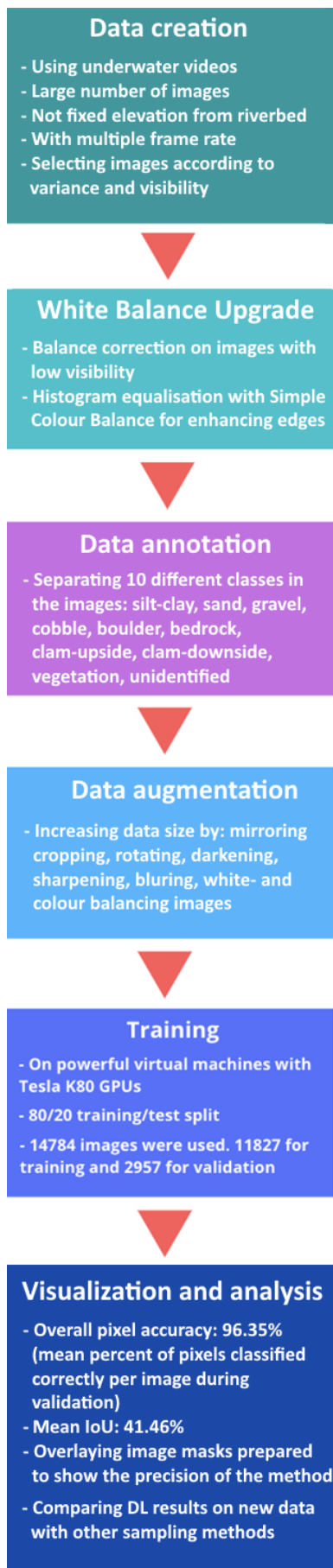
257 The video recordings were made with a GOPRO Hero 7 and a Hero 4 commercial action cameras. Image
 258 resolutions were set to 2704x2028 (2.7K) with 60 frame per second (fps) and 1920x1080 (1080p) with 48 fps,
 259 respectively. Other parameters were left at their default (see GOPRO 2014; 2018), resulting in slightly different
 260 quality of produced images between the two cameras. We found that a 0.2-0.45 m/s vessel speed with 60 fps
 261 recording frequency was ideal to retrieve satisfactory images in a range of 0.4-1.6 m camera-bed distances. This
 262 meant approximately 15 minutes long measurements per transects. Further attention needed to be paid to the reel
 263 and its cable during the crossing when the equipment was on the upstream side of the boat. If the flow velocities
 264 are relatively high (compared to the total submerged weight of the underwater equipment), the cable can be pressed
 265 against the vessel-body due to the force from the flow itself, causing the reel cable to jump to the side and leave
 266 its guide. This results in the equipment falling to the riverbed and the measurement must be stopped to reinstall
 267 the cable. For illumination, a diving light with 1500 lumen brightness and 75° beam divergence, and one with
 268 1800 lumen and 8° were used. The four lasers for scaling had 450-520 nm (purple and green) wavelength and 1-
 269 5 mW nominal power. Power supply was ensured with batteries for all instruments.

270
 271 At Site A and Site B, conventional bed material (physical) samplings were also carried out by a grabbing (bucket)
 272 sampler along the analysed transects. At each cross-section 4-5 samples were taken, with one exception where we
 273 had 10. The measured GSDs were used to validate results of the AI algorithm. Separately, a visual evaluation of
 274 the videos was also carried out, where a person divided the transects into subsections based on their dominant
 275 sediment classes, after watching the footages.

276 **2.3 Image analysis: Artificial Intelligence and the wavelet method**

277 In this study, we built on the former experiences of the authors, using Benkó et al., 2020 as a proof-of-concept,
278 where the developed algorithm was applied for analysing drone videos of a dry riverbed. The same architecture
279 was used in this manuscript, which is based on the widely used Google's DeeplabV3+ Mobilenet, in which many
280 novel and state-of-the-art solutions are implemented (e.g., Atrous Spatial Pyramid Pooling; Chen et al., 2018).
281 The model was implemented with Pytorch, exploiting its handy API and backward compatibility. The main goal
282 was to build a deep neural network model which can recognise and categorise (via semantic segmentation; Chen
283 et al., 2018) at least three main sediment size classes, i.e., sand, gravel and cobble, in the images, while being
284 quickly deployable. The benefit of the introduced method compared to conventional imagery methods lies in the
285 potential of automation and increased speed. If the annotation and training is carried out thoroughly, analysing
286 further videos can run effortlessly, while the computation time can be scaled down either vertically (using stronger
287 GPUs) or horizontally (increasing the number of GPUs; if parallel analysis of images is desired). In this study a
288 TESLA K80 24GB GDDR5 348bit GPU, an Intel Skylake Intel® Xeon® Gold 6144 Processor (24.75M Cache,
289 3.50 GHz) CPU with 13GB RAM was used. Also, contrary to other novel image-processing approaches in riverine
290 sediment research (Buscombe, 2013; Detert and Weitbrecht, 2013), the deep convolutional neural network is
291 much less limited by image resolution and mm/pixel ratios, because it does not rely on precise pixel count. This
292 is an important advantage to be exploited here, as we perform non-scaled training and measurements with the DL,
293 i.e., camera-bed distance constantly changed, and size-reference was not used in the images by the DL.

294
295 Fig. 4 presents the flowchart of our DL-based image processing methodology. The first step after capturing the
296 videos was to cut them into frames, during which the videos were exploded into sequential images. Our
297 measurement setup proved to be slightly nose-heavy. Due to this, and the drag force combined, the camera tilted
298 forward during the measurements. As a result, the lower parts of the raw images were sometimes too dark, as the
299 camera was looking over the riverbed, and not at the lit part of the bed. In this manuscript, this problem was
300 handled by simply cutting out the lower 25% of the images as this was the region usually containing the dark,
301 unlit areas. Brightening and sharpening filters were applied on the remaining part of the images to improve their
302 quality. Next, the ones with clearest outlines and best visibility were chosen. This selection process was necessary
303 because this way the delineation process (learning the prominent characteristics of each class) can be executed
304 accurately, without the presence of misleading or confusing images, e.g., blurry or dark pictures where the features
305 are hard to recognise. For training purposes, we chose three videos from different sections each being ~15 minutes
306 long with 60 fps and 48 fps, resulting in 129 600 frames. In fact, such a large dataset was not needed due to the
307 strong similarity of the consecutive frames. The number of images to be annotated and augmented were therefore



decreased to ~2000. We also performed a white balance correction on some of the images to improve visibility, making it even easier to later define the sediment class boundaries. We used an additional algorithm to generate more data, with the so-called Simplest Colour Balance method (Limare et al., 2011). It is a simple, but powerful histogram equalisation algorithm which helps to equalise the roughness in pixel distribution.

These steps were followed by the annotation, where we distinguished ten classes: silt-clay, sand, gravel, cobble, boulder (mainly riprap), bedrock, clam-upside, clam-downside, vegetation, unidentified (e.g., wreckages). Annotation was carried out by a trained personnel, not by the authors, and performed with the help of an open-source software called PixelAnnotationTool (Breheret, 2017), which enables the user to colour mask large parts of an image based on colour change derivatives (i.e., colour masking part of the images which belong to the same class, e.g., purple/red – sand, green – gravel, yellow – cobble, etc.). The masks and outlines were drawn manually, together with the so-called watershed annotation. That is, when a line was drawn, the algorithm checked for similar pixels in the vicinity and automatically annotated them with the same class. The annotation was followed by a data augmentation step where beside mirroring, cropping, rotating the images (to decrease the chance of overfitting), we also convolved them with different filters. These filters added normally distributed noise to the photos to influence the watershed algorithm and applied sharpening, blurring, darkening, and white balance enhancement. Thus, at the data level, we tried to ensure that any changes in water purity, light, and transparency, as well as colour changes, were adequately represented during training. Images were uniformly converted to 960x540 resolution, scaling them down to make them more usable to fit in the GPU's memory. The next step was to convert all the images from RGB (Red-Green-Blue) based colour to grayscale. This is important because colour images have 3-channels, so that they contain a red, a green, and a blue layer, while grayscale images' pixel can only take one value between 0 and 255. With this colour conversion we obtained a threefold increase in computational speed. In total, a dataset of 14,784 human-annotated images was prepared (from the ~2000 images of the 3 training videos). The next step was to separate this dataset into training and validation sets. In this study, 80% of it was used for training the Deep Learning algorithm, while 20% was withheld and reserved for the validation of the training. It was important to mix the images so that the algorithm selects batches in a pseudorandom manner during training, thus preventing the model from being overfitted.

Figure 4: Flowchart of the applied methodology.

348 Finally, after several changes in the hyperparameters (i.e., tuning), the evaluation and visualisation of the training
349 results were performed. Tuning is a general task to do when building Deep Learning Networks, as these
350 hyperparameters determine the structure of the network and the training process itself. Learning rate, for example,
351 describes how fast the network refreshes, updates itself during the training. If this parameter is set too high, the
352 training process finishes quickly, but convergence may not be reached. If it is too low, the process is going to be
353 slow, but it converges. For this reason, nowadays the learning rate decay technique is used, where one starts out
354 with a large learning rate, then slowly reduces it. The technique generally improves optimization and
355 generalization of the Deep Learning Networks (You et al., 2019). In our case, learning rate was initialised to 0.01,
356 with 30000 iteration steps, and the learning rate was reset after every 5000 iterations with a decay of 0.1. Another
357 important parameter was the batch size, which sets the number of samples fed to the network before it updates
358 itself. Theoretical and empirical evidence suggest that learning rate and batch size are highly important for the
359 generalization ability of a network (He et al., 2019). In our study, a batch size of 16 was used (other general values
360 in the literature are 32, 64, 128, 256). We used a cross-entropy loss function.

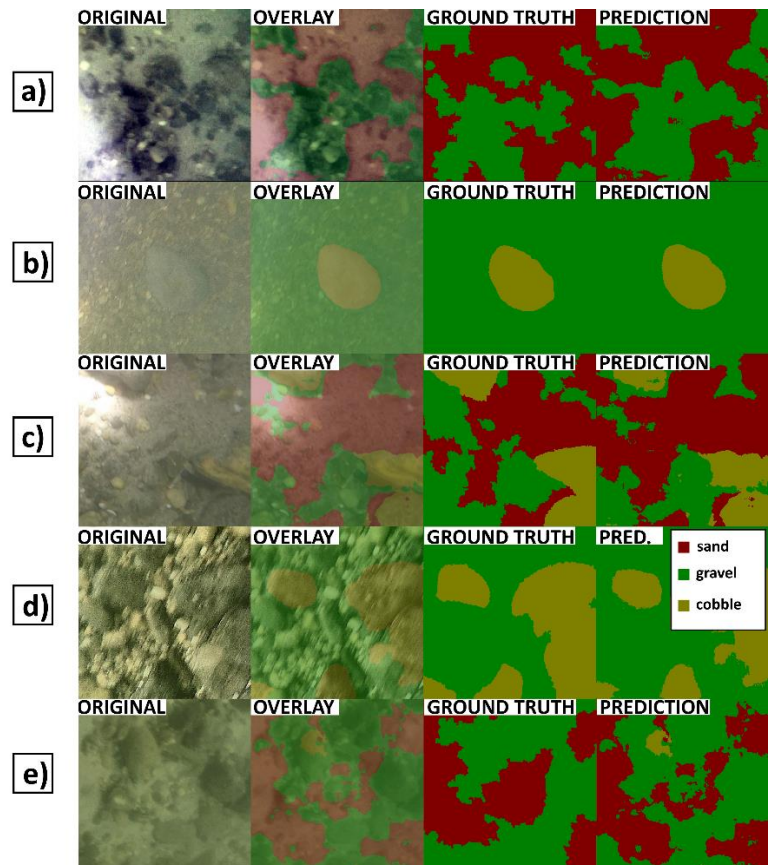
361
362 As previously mentioned, the training of the DL algorithm was managed without scaling, without the need for
363 equipped lasers. However, we intended to use the laser pointers to provide a spatial scale for the recorded videos,
364 as a secondary validation. As the lasers were not functioning as we originally hoped, we could not use them
365 constantly during the cross-sectional surveys and could not aim for transactional scaling and validation this way.
366 Instead, we diverted to validation in the points of the physical samplings as we could use the lasers in a few,
367 selected points only. We used a textural image-processing method to analyse the video images of these sampling
368 spots. For this, the already mentioned, transferable wavelet-based signal- and image-processing method was
369 chosen. The method enables to calculate the image-based grain size distribution of the selected pictures. The grey-
370 scale intensity is analysed through pixel-rows and -columns of the image and handled as individual signals. Then,
371 instead of Fourier-transform, the less-constrained wavelet-transform is applied to decompose them. Finally,
372 calculating the power spectra and the sizes (from pixel to millimetre, using the scale) of the wavelet components
373 (each wavelet describes an individual grain) produces the grain size distribution for the given image. Beforehand,
374 this method was proved to be the most efficient, non-DL image-processing method for mixed sediments
375 (Buscombe, 2013; 2020) and was already tested for underwater circumstances in an earlier study (Ermilov et al.,
376 2020).

377 **3 Results and discussion**

378 **3.1 Evaluation of the training**

379 To evaluate the training process, the 2957 images of the validation set were analysed by the developed Deep
380 Learning algorithm and the given DL-results were then compared to their human-annotated counterparts. Fig. 5a-
381 d shows results of original images (from the validation set), their ground truth (annotation by the training
382 personnel), as well as the DL prediction (result of the model). The overlays of the original and the predicted
383 images are also shown for better visualization. Calculating the overall pixel accuracy (i.e., the percent of pixels
384 that were correctly classified during validation) returned a satisfactory result with an average 96% match (over
385 the 2957 validation images, each having 960x540 resolution, adding up to a total of 1 532 908 800 pixels as

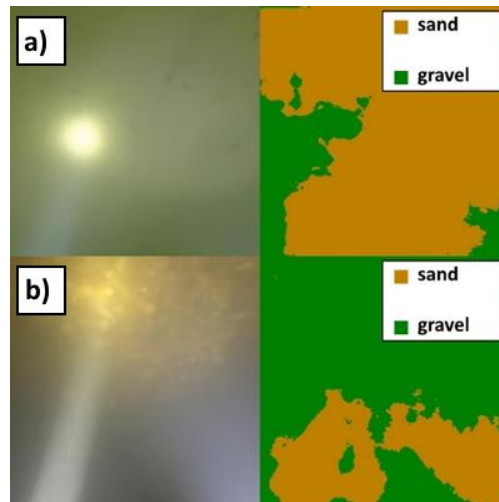
386 100%). As this parameter in object detection and Deep Learning is not a stand-alone parameter (i.e., it can still be
 387 high even if the model performs poorly), the mean IoU (intersection-over-union or Jaccard index) was also
 388 assessed, indicating the overlap of ground truth area and prediction area, divided by their union (Rahman and
 389 Wang, 2016). This parameter showed a much slighter agreement of 41.46%. Interestingly, there were cases, where
 390 the trained model gave better result than the annotating personnel. While this highlighted the importance of
 391 thorough and precise annotation work, it also showcased that the number of poor annotations was relatively low,
 392 so that the algorithm could still carry out correct learning process and later detections, while not being severely
 393 affected by the mistake of the training personnel. Fig. 5e showcases an example for this: the correct appearance
 394 of cobble (yellow) in the prediction, even though the user (ground truth) did not define it during annotation. As a
 395 matter of fact, these false errors also decrease the IoU evaluation parameter, even though they increase the
 396 performance of the DL algorithm on the long term. Hence, this shows that pure mathematical evaluation may not
 397 describe the model performance entirely. Considering that others also reported similar experience with Deep
 398 Learning (Lu et al., 2018) and the fact that 40% and 50% are generally accepted IoU threshold values (Yang et
 399 al., 2018; Cheng et al., 2018; Padilla et al., 2020), we considered the 41.46% acceptable, while noting that the
 400 annotation and thus the model can further be improved. The general quality of our underwater images may have
 401 also played a role in lowering the IoU result.
 402



403
 404 **Figure 5: a-d) Example comparisons of ground truth (drawn by the annotating personnel, 3rd column) and DL**
 405 **predicted (result of analysing the raw image by the previously trained DL model, 4th column) during the validation**
 406 **process. The 1st column shows raw images, while the 2nd column overlays the result of the DL detection on the raw**
 407 **image for better visual context. e) Example of training personnel mistake during the annotation (i.e., lack of**
 408 **cobble/yellow annotation in ground truth) and how the DL performed better by hinting at the presence of the cobble**
 409 **fraction, leading to a false negative result during validation.**

410
411
412
413
414
415
416
417
418

One of these quality issues for the DL algorithm was associated with the illumination. Using a diving light with small beam divergence proved counterproductive. The high intensity, focused light occasionally caused overexposed zones (white pixels) in the raw bed image, misleading the DL algorithm and resulting in detection of incorrect classes there (Fig. 6a). In darker zones, where the suspended sediment concentration was higher and at the same time, the effect of camera tilting was not completely removed by preprocessing, the focused light sometimes reflected from the suspended sediment itself and resulted in brighter patches in the images (Fig. 6b). This also caused false positive detections.



419
420
421

Figure 6: The effect of strong diving light on the DL algorithm. a) Purely sand covered zone. b) Darker zone with higher SSC. The original images are on the left, while the DL detections can be found on the right.

422

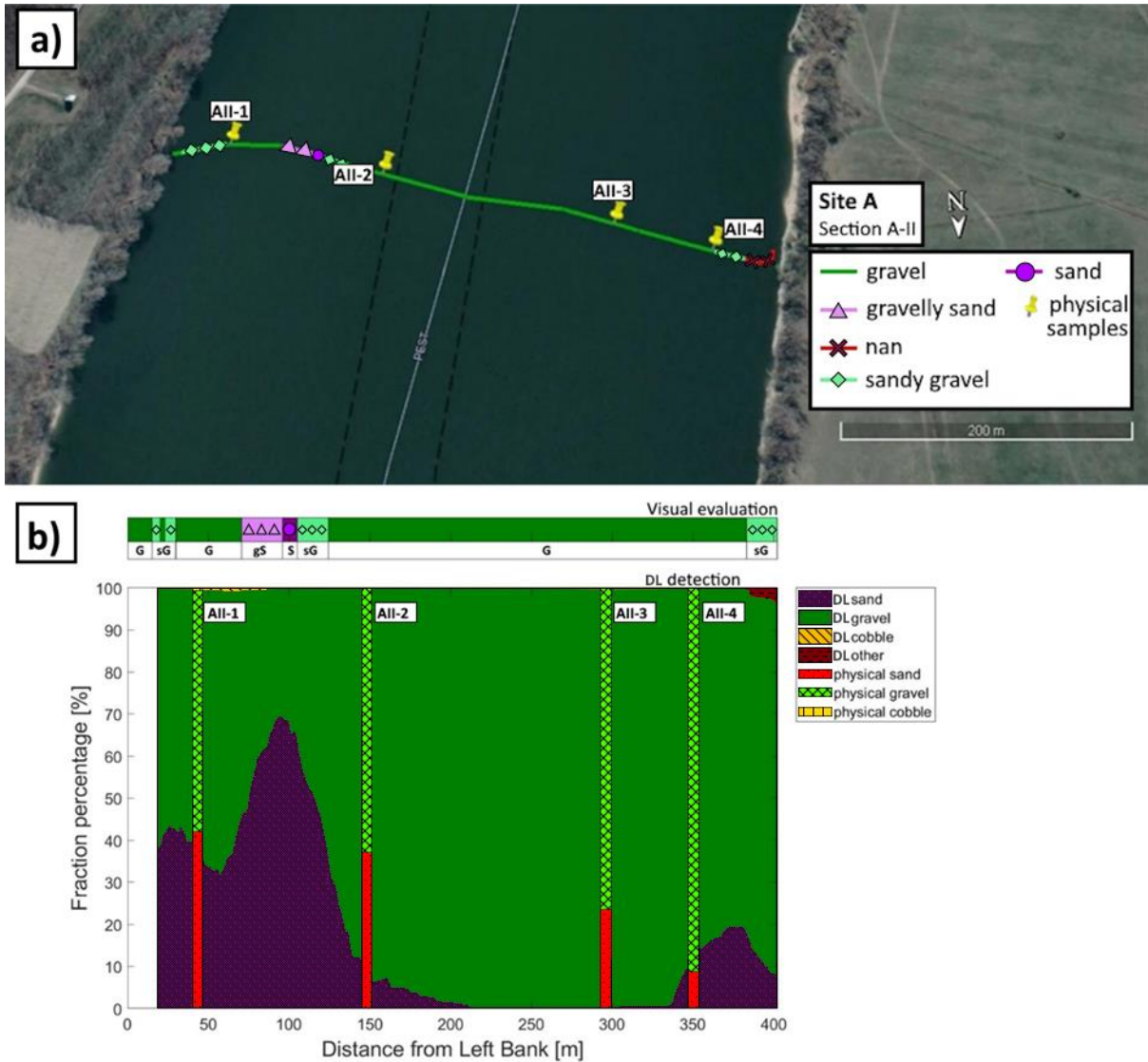
423 3.2 Comparison of methods

424
425
426
427
428
429
430
431
432
433
434
435
436

In each masked image, the occurring percentage of the given class (i.e., the percentage of the pixels belonging to that class/colour mask, compared to the total number of pixels in the image) was calculated and used as the fraction percentage in that given sampling point. These sediment classes reconstructed by the DL algorithm were then compared to three alternative results: i) visual estimation, ii) GSD resulted from conventional grab sampling, iii) wavelet-based image-processing. In the followings, results from two cross-sections will be highlighted, one from Site A, the video used for the training, and one from Site B, being new for the DL. An averaging window of 15 m was applied on each cross-sectional DL result to smoothen and despike the dataset. The interval of physical sample collection in wider rivers can range anywhere between 20-200 m within a cross-section, depending on the river width and the homogeneity of riverbed composition. The averaging window size was chosen to be somewhat lower than our average applied physical sampling intervals in this study, but still in the same order of magnitude. The scope of the present manuscript did not include further sensitivity analysis of the window size. In the followings, the reader is led through the comparison process via the example of two transects, and is given the over-all evaluation of the accuracy of the method.

437 3.2.1 Visual evaluation and physical samples

438 In Fig. 7a, the path of the vessel can be seen in Section A – II, at Site A. The path was coloured based on the visual
439 evaluation of the riverbed images. The different colours represent the dominant sediment type seen at the given
440 point of the bed. The locations of the physical bed material samplings are also shown (see yellow markers). App.
441 Fig. A1 presents the raw (i.e., before moving-average) results of the DL detection of each analysed image along
442 Section A – II. Currently, our approach is sensitive and large spikes, differences can occur in the DL detection
443 between consecutive, slightly displaced video frames. Due to this, and the fact that there is uncertainty in the
444 coordinates of the underwater photos and their corresponding physical samples, it is not recommended to carry
445 out comparisons by selecting certain image and its DL detection. Instead, we applied a moving average-based
446 smoothing for each raw, cross-sectional DL detection, with a window-size corresponding to 15 m at each site.
447 These moving-averages are later used to compare in the sampling points to the physical sampling and the wavelet
448 method. For illustration purposes, we provided the raw DL detections of all the sampling point images in the
449 Appendix, even though their result may not be representative of their corresponding moving-average values. Fig.
450 7b shows the cross-sectional visual classification compared to the DL-detected sediment fractions in percentage
451 after applying moving-average (i.e., the smoothed version of App. Fig. A1). The noises are mostly caused by
452 sudden changes in lighting conditions. It happens either from losing visual on the riverbed momentarily due to
453 sudden topography changes or from increased suspended sediment concentration. The DL result shows
454 satisfactory match with the human evaluation. For example, around 100 m from the left bank, between AII-1 and
455 AII-2 sampling points, the DL algorithm peaks with around 70% sand and 30% gravel correctly. Furthermore, on
456 the two side of this peak a steep transition to gravel and decreasing sand occurs, similarly to the visual observation,
457 marked as sandy gravel and gravelly sand. Mixed sediment zones were also correctly identified by the DL
458 algorithm at both riverbanks.
459



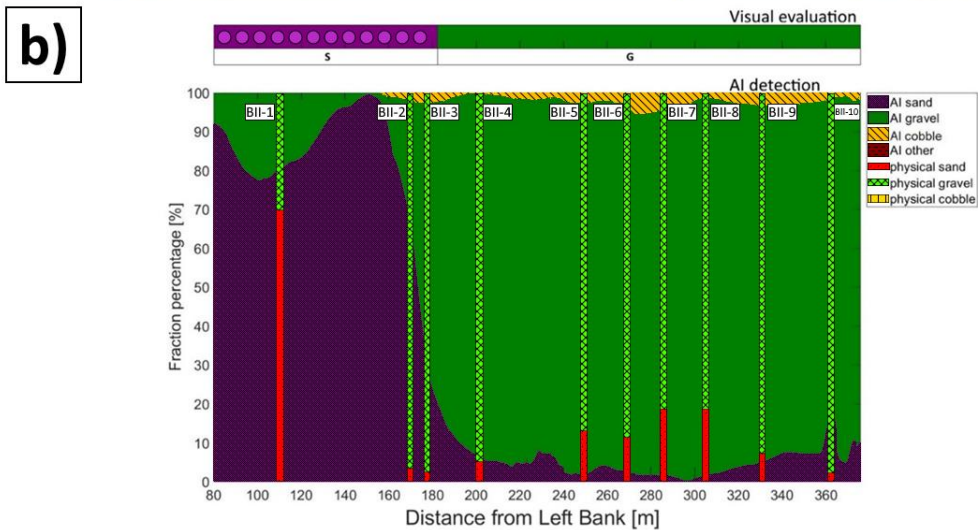
460

461 **Figure 7: a) The path of the vessel and camera in Section A – II, Site A. The polyline is coloured based on the sediment**
 462 **features seen during visual evaluation of the video. Yellow markers are the locations of physical bed material samplings.**
 463 **(Map created with Google Earth Pro). b) The visual evaluation of the dominant sediment features in the video (top)**
 464 **compared to sediment fraction percentage, recognised by the DL algorithm (bottom). DL result after applying moving-**
 465 **averaging. The visual evaluation included four classes: gravel – G, sandy gravel – sG, gravelly sand – gS, sand – S,).**
 466 **The fractions of the physical samples are shown as verticals.**

467

468 At site B (Fig. 8a) the river morphology is more complex compared to Site A as a groyne field is located along
 469 the left bank (see Fig. 2b). As such, the low flow regions between the groynes yield the deposition of fine
 470 sediments, and much coarser bed composition in the narrowed main stream. As it can be seen, the DL algorithm
 471 managed to successfully distinguish these zones: the extension of fine sediments in the deposition zone at the left
 472 bank were adequately estimated and showed a good match with the visual evaluation for the whole cross-section
 473 (see Fig. 8b).

474



475
 476 **Figure 8: a) The path of the vessel and camera in Section-B - II, Site B. The polyline is coloured based on the sediment**
 477 **seen during visual evaluation of the video. Yellow markers are the locations of physical bed material samplings. (Map**
 478 **created with Google Earth Pro). b) Sediment fraction percentages in Section-B - II, recognised by the AI. The visual**
 479 **evaluation included two classes: gravel – G, sand – S). The fractions of the physical samples are shown as verticals.**

480
 481 Results of the other measurements can be found in the Appendix. App. Fig. C2, D2 and E2 show that the trend of
 482 riverbed composition from the visual evaluation is well-captured by the DL algorithm in the other cross-sections
 483 of the study as well.

484
 485 Next, the physically measured and DL-detected relative proportion of sand, gravel and cobble fractions were
 486 compared in each of the 27 sampling points. Firstly, however, outliers had to be identified. In our case, this meant
 487 the separation of sampling points where the differences between the results of the two methods were independent
 488 from the efficiency and performance of the DL algorithm. This selection was carried out after analysing the
 489 grainsize distribution curves of the weight-sieved physical samples (App. Fig. F1) and the riverbed images at the
 490 sampling points (App. Fig. A3, B1, C4, D4, E4). Based on our findings, the outliers have been identified and

491 separated into Outlier Type A, and Outlier Type B categories. First category included the sampling points where
 492 the GSD curves showcased bimodal (gap graded) distributions. This type of riverbed sediment distribution is a
 493 typical sign of riverbed armouring (Rákóczi, 1987; Marion & Fraccarollo, 1997), where a coarse surface layer
 494 protects the underlying finer subsurface substrate (see e.g., Wilcock, 2005). While the camera only sees the upper
 495 layer, the bucket sampler can penetrate the surface and gather sample from the subsurface as well. As a result, the
 496 two methods cannot be compared solely on the surface distribution. In App. Fig. A2, supportive images of bed
 497 armouring are provided, taken during our surveys in the Upper section of the Hungarian Danube. Out of the 27
 498 sampling points, 11 was categorised as Outlier Type A. The category of Outlier Type B consisted of points from
 499 the opposite case: where the riverbed image contained fine sediment, but the physical samples did not. In these
 500 cases, a relatively thin layer of fine sediment covered the underlying gravel particles. 2 sampling points were
 501 categorised as Outlier Type B, both of which were near to the borderline between a deposition zone behind a
 502 groyne, and the gravel bedded main channel. In these cases, the bucket sampler probably either stirred up the
 503 deposited fine sediment and washed it down during its lifting or was dragged through purely gravel bedded patch
 504 during sampling, as the surface composition was rapidly changing on this before-mentioned borderline. It is also
 505 worth noting that the physical samples are analysed by weighing the different sediment size classes, resulting in
 506 weight distribution. On the other hand, the imagery methods provide surface distributions, hence having a thin
 507 layer of fine sediments on the top can strongly bias the resulted composition (Bunte and Abt, 2001; Sime and
 508 Ferguson, 2003; Rubin et al., 2007).

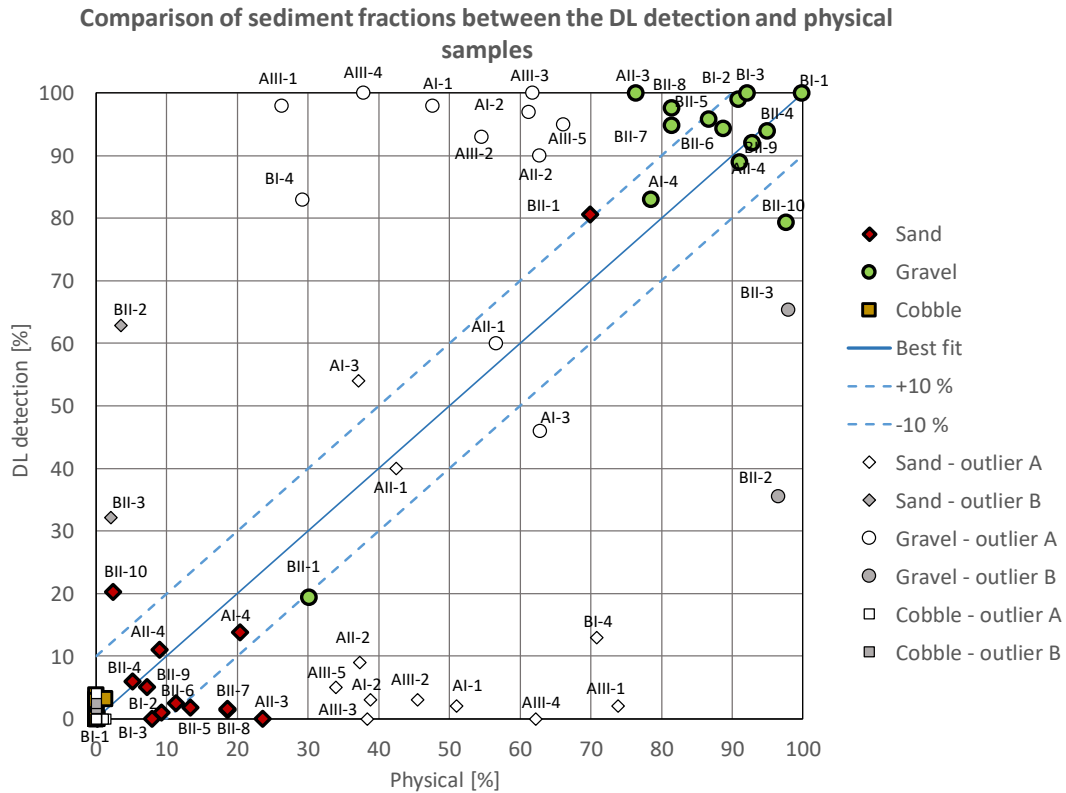
509

	Comparable data	Outlier Type A	Outlier Type B	Σ
No. sampling points	14	11	2	27

510 **Table 2: After evaluating the results of the sieving analyses and riverbed surface images, out of the 27 sampling points,**
 511 **14 were defined as comparable between the applied sampling methods. 11 points were categorised as Outlier Type A,**
 512 **because their GSD curves were bimodal. 2 points were defined as Outlier Type B, since their images showed the**
 513 **presence of fine sediment, while the sieve analyses did not.**

514

515 Overall, the DL-based classification agreed well within the comparable sampling points, with an average error of
 516 4.5% (Fig. 9). It can be seen that even though in outlier points AII-1 and AI-3 the DL algorithm coincidentally
 517 gave good match with the sieving analysis, in the rest of the outlier points the DL- and physical-based results
 518 systematically differ from each other, supporting our outlier selection methodology.



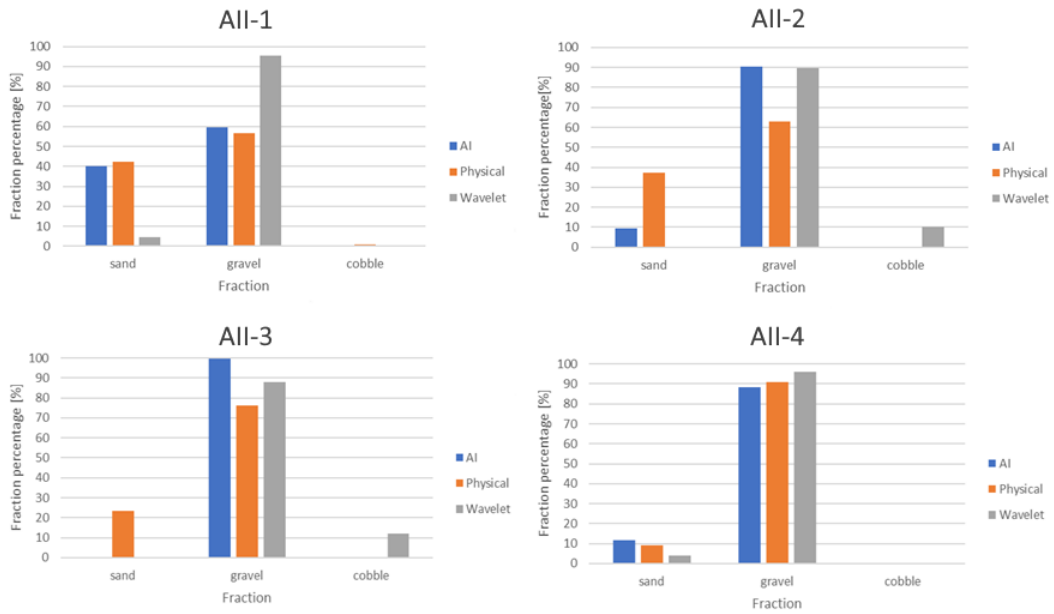
519
 520
 521
 522
 523
 524
 525

Figure 9: Comparison of relative sediment fractions between the DL detection and physical samples. The three main sediment types (sand-gravel-cobble) are marked with different colour and symbols. The name of the sampling points where the given relative proportion was measured/detected is also written for gravel and sand (cobble was negligible). The proportions of outlier sampling points are marked with white/grey, while the symbol represents the sediment type respectively. The comparable points have their proportions with green (gravel) and red (sand) symbols.

526 **3.2.1 Wavelet analysis**

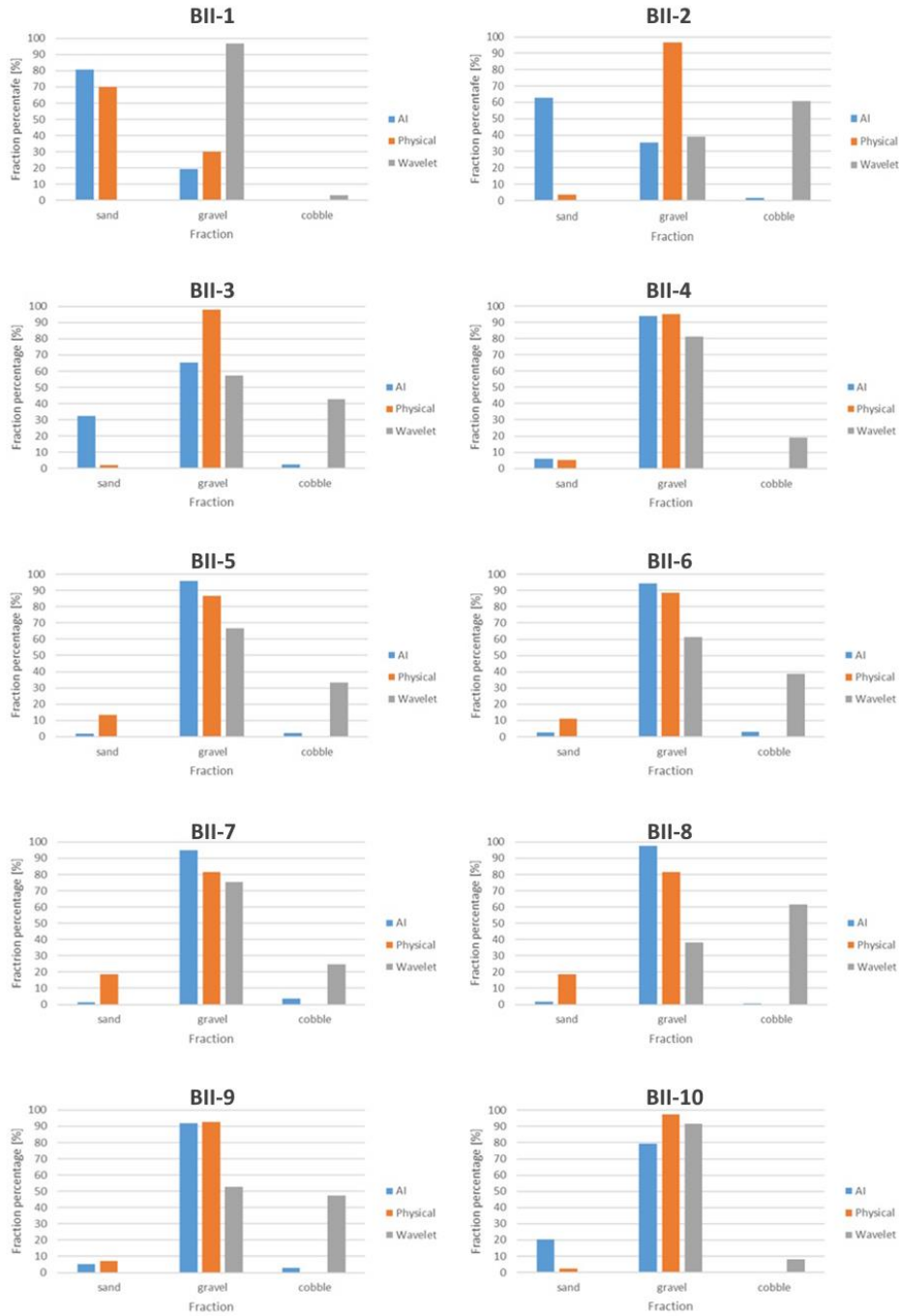
527 As for the wavelet analysis-based imagery technique, an overall slight overestimation of the coarse particles can
 528 be observed, and the sand classes are, in fact, not reconstructed correctly. This finding agrees well with the field
 529 experiences of Ermilov et al. (2020), where the authors indicated the strong sensitivity of the wavelet technique
 530 on the image resolution, and showed that to detect a grain, the diameter must be at least three times larger than
 531 the pixel. In the following, the wavelet-detected relative sediment proportions are compared to the earlier,
 532 corresponding DL-, and physical based ones via bar plots (Fig. 10, 11). For example, the camera was closer to the
 533 riverbed at sampling points AII-1 and AII-4, resulting in a better mm/pixel ratio, hence the wavelet algorithm was
 534 able to detect coarse sand, but finer sand was neglected yielding the lower sand percentages (Fig. 10). In the other
 535 sampling points, where sand was below its resolution, the wavelet method systematically measured the presence
 536 of cobbles instead (Fig. 10), even though the other two methods did not. This trend generally described the
 537 performance of the wavelet method during our study. For visual purposes, an example of the difference in the
 538 capabilities of the two method is given in Fig. 12. While both detected the presence of two major sediment
 539 categories, the wavelet translated the information as gravel and cobble mixture, meanwhile the DL algorithm
 540 recognised the sand coverage and gravel particles.

541



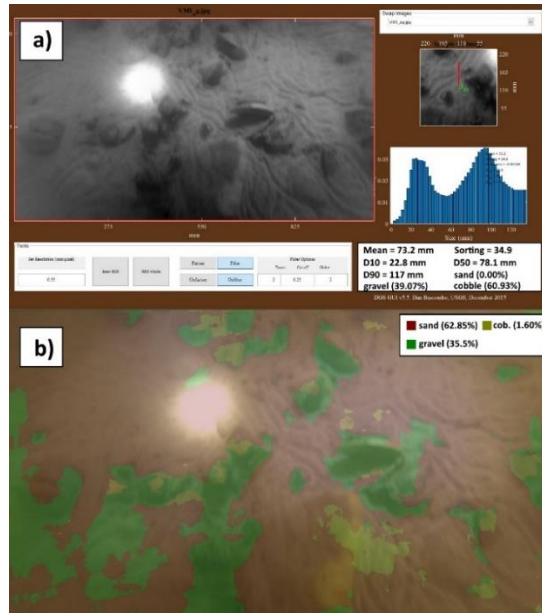
542
 543 **Figure 10: Comparison of relative sediment fraction proportions [%] at the sampling locations from the moving-**
 544 **averaged DL detection, conventional sieving and the wavelet-based image processing method. Section A – II.**

545



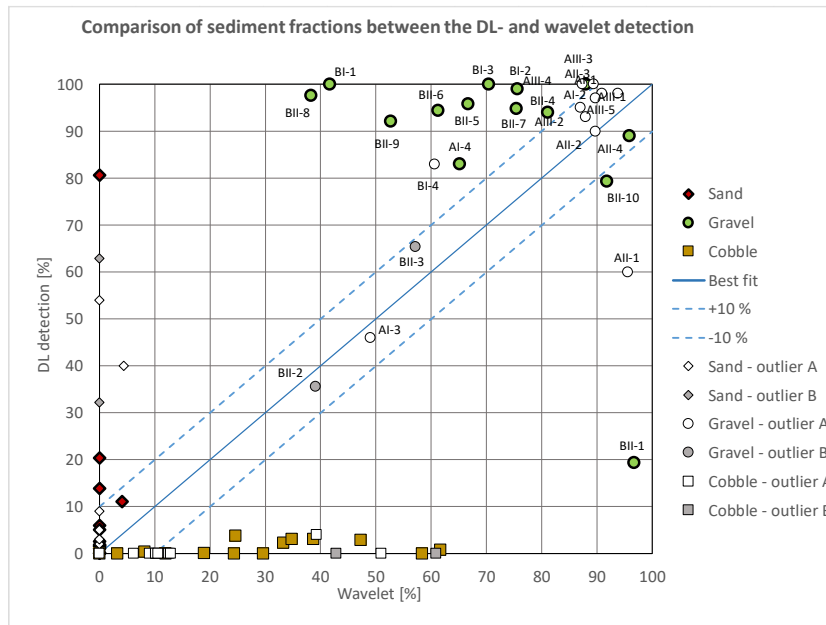
546
547
548

Figure 11: Comparison of relative sediment fraction proportions [%] at the sampling locations from the moving-averaged DL detection, conventional sieving and the wavelet-based image processing method. Section-B - II.



549
 550 **Figure 12: a) Wavelet analysis result of the underwater image in BII-2. b) DL detection result of the same image.**

551
 552 Overall, the comparison between the two image-based method showed greater discrepancies (Fig. 13), due to the
 553 limitations of the wavelet approach, discussed earlier. The same sampling points were labelled as outliers as
 554 earlier. As it can be seen, the wavelet significantly differed in the points where the physical samples and DL-
 555 detections matched (green data points), due to its excessive, false cobble detections. However, it showed good
 556 agreement with the DL in most of the outlier points, supporting the earlier observation: the surface in those points
 557 was composed of solely gravel, and the finer fractions of the physical samples must have come from the
 558 subsurface. Hence, the outlier selection process was well based.



559
 560 **Figure 13: Comparison of sediment fractions between the DL detection and the wavelet approach, for the selected**
 561 **sampling points. The three main sediment types (sand-gravel-cobble) are marked with different colour (red-green-**
 562 **yellow) and symbols (diamond-circle-square) respectively. The name of the sampling points where the given relative**
 563 **proportion was measured/detected is also written for gravel. The proportions of outlier sampling points are marked**
 564 **with white/grey, while the symbol represents the sediment type respectively. The comparable points have their**
 565 **proportions with green (gravel), red (sand) symbols.**

566
567 Based on the results presented in this manuscript, it could be established that the DL algorithm managed to
568 recognise the main features of the riverbed material composition from underwater videos with satisfactory
569 accuracy in the comparable sampling points (based on the sieving analysis of physical samples) and along cross-
570 sections (based on the visual evaluation). The method showed good potential for mapping heterogenous riverbeds
571 along river cross-sections. Furthermore, the wavelet proved to be a limited comparison tool with the introduced
572 field measurement methodology, as this latter did not provide it with the sufficient resolution most of the time.
573

574 **3.3 Implementation challenges**

575 The power supply for the entire imaging infrastructure, i.e., for the camera, the diving lights and lasers, was
576 ensured by batteries. However, due to the low temperature at the river bottom, the battery level decreased
577 extremely fast, compared to normal circumstances. Providing the power supply directly from the motorboat can
578 overcome this issue. Keeping the camera in the adequate height also caused difficulties, since getting too close to
579 the bed can harm the devices, lifting too high, on the other hand, will result in poor image quality. The measured
580 instantaneous ADCP flow depth data was used therefore to keep the bed in camera sight, while maintaining proper
581 boat velocity to avoid blurry images. Choosing a higher recording frequency and decreasing exposure time,
582 however, can be beneficial and alter this limitation, when provided. Lower velocities could not be maintained as
583 the river would have moved the vessel out of the section. An alternative solution can be to move on longitudinal
584 (streamline) paths instead of transects. This would allow for lower vessel speed. This would increase the time of
585 the measurement, which still could be profitable if the images are of higher quality. However, the conventional
586 way for river bathymetry surveys is to move on transversal, cross-sectional paths, due to the river bathymetry
587 having a lower spatial variation along streamlines, compared to the changes that occur in the transversal direction
588 (Benjankar et al., 2015; Kinsman, 2015). As such, it may require carrying out a relatively dense set of longitudinal
589 paths to gain proper information, further increasing the time demand. Thus, for this alternative, higher attention
590 needs to be paid towards choosing these paths and the interpolation method. Another challenge can be the
591 influence of drag force on the measurement setup. In our case, even though the main body itself was a streamlined
592 weight, equipping the other tools on it turned the setup geometry irregular. Additionally, we found that our setup
593 was a bit nose-heavy. On the long term however, this effect could be reduced by building a streamlined container
594 (e.g., 3D-printed body, or a body similar to unmanned underwater vehicles') with slots in it for each device, and
595 also by improving the weight distribution. Furthermore, we hypothesize that by using lasers (as originally planned
596 in this study) during the measurements, the known structure (i.e., the position and distances) of the laser points'
597 projection when the setup is perpendicular to the bed, can help to orthorectify the images. This will decrease the
598 effect of occasional tilting when one wishes to carry out size analysis on the images. In our case, we presented
599 how the wavelet method had inherently bigger issues (i.e., image resolution limit) when used with the introduced
600 methodology, which could not be caused by the tilting of the camera since those would be in a significantly lower
601 magnitude of error.

602
603 As for the training of the DL algorithm with the underwater images, the illumination is indeed a more crucial
604 aspect, compared to normal imagery methods. In many cases only the centre areas of the images were clearly
605 visible, whereas the remaining parts were rather dark and shady. Determining the boundaries between distinct

606 sediment classes for these images was challenging even for experienced eyes. This quality issue generated
607 incorrect annotations at first. To overcome this issue, manually varying the white balance thus enhancing the
608 visibility of the sediment could improve the results of the training. It is known that when Deep Learning methods
609 are to be used, most of the problems arise from the data side (Yu et al., 2007), whereas issues related to the applied
610 algorithms and hardware are rare. This is because data is more important from an accuracy perspective than the
611 actual technical infrastructure (Chen et al., 2020). The time demand of image annotation (data preparation) is
612 relatively high, i.e., a trained person could analyse roughly 10 images per hour. On the other hand, as introduced
613 earlier, a great advantage of using DL is the capability of improving the quality of training itself, often yielding
614 better agreement with reality, compared to the manual annotation. Similar results have been reported by Lu et al.,
615 (2018). This at the same time proves that with the introduced approach, there is no need for very precise manual
616 training, thus a fast and effective training process can eventually be achieved.

617

618 The validation of the Deep Learning algorithm is far from straightforward. In this study, four approaches were
619 adapted, a mathematical approach, and comparison with three other measurement methods, respectively. The
620 mathematical approach was based on calculating pixel accuracy and the Intersection-over-union parameter, as it
621 is usually done in case of Deep Learning methods to describe their efficiency (e.g., Rahman and Wang, 2016).
622 However, the DL model in some cases overperformed, and provided more accurate results for the sediment
623 composition than the human annotator did. This meant the calculated difference between the annotated validation
624 images and their responding DL-generated result was not solely originated from underperformance of the DL-
625 model, but from human error as well. Consequently, using only the mathematical evaluation in this study could
626 not describe adequately the model performance. Hence, the results were compared to those of three other methods:
627 i) visual evaluation of the image series, ii) a wavelet-based image-processing method (using the method of
628 Buscombe, 2013) and iii) riverbed composition data from physical samples. Considering the features of the
629 applied methods, the first one, i.e., the visual observation, is expected to be the most suitable for the model
630 validation. Indeed, when assessing the bed surface composition by eye, the same patterns are sought, i.e., both
631 methods focus on the uppermost sediment layer. On the other hand, the physical sampling procedure inherently
632 represents subsurface sediment layers, leading to different grain size distributions in many cases. For instance, as
633 shown earlier, if bed armour develops in the riverbed and the sampler breaks-up this layer, the resulted sample
634 can contain the finer particles from the subsurface. On the contrary, in zones where a fine sediment layer is
635 deposited on coarse grains, i.e., a sand layer on the top of a gravel bed, the physical samples represent the coarse
636 material too, moreover, considering that the sieving provides weight distribution this sort of bias will even enhance
637 the proportion of the coarse particles. Attempts were made to involve a third, wavelet-based method for model
638 validation. However, this method failed when finer particles, i.e., sand, characterized the bed. This is an inherent
639 limitation of these type of methods, as discussed earlier, i.e., when the pixel size is simply not fine enough to
640 reconstruct the small grain diameters in the range below fine gravel. Lastly, the most comparable sample points
641 were selected to quantify the performance of the DL. Holding the sieved physical samples as ground truth, the DL
642 algorithm showed promising results. The average error (difference) between DL-detected and physically
643 measured relative sediment fraction portion percentages was 4.5%. Furthermore, the DL algorithm successfully
644 detected the trend of changing bed composition along complete river cross-sections.

645

646 As it is known, the ML and DL models can learn unknown relationships in datasets, but unwanted biases as well.
647 With our current dataset, these biases would be the darker tones of visible grain texture and the lack of larger grain
648 sizes. This way our model in its current state is only applicable effectively in the chosen study site, until the dataset
649 is not expanded with additional images from other rivers or regions. However, the purpose of the manuscript was
650 to introduce the methodology itself and its potential in general and not to create a universal algorithm.

651 **3.4 Novelty and future work**

652 The introduced image-based Deep Learning algorithm offers novel features in the field of sedimentation
653 engineering. First, to the authors' knowledge, underwater images of the bed of a large river have not yet been
654 analysed by AI. Second, the herein introduced method enables extensive mapping of the riverbed composition, in
655 contrast to most of the earlier approaches, where only several points or shorter sections were assessed with
656 imagery methods. Third, the method is much faster compared to conventional samplings or non-DL-based image-
657 processing techniques. The field survey of a 400 m long transect took ~15 minutes, while the DL analysis took 4
658 minutes (approx. 7 image/s). The speed range of 0.2-0.45 m/s of the measurement vessel and the 15 minutes per
659 transect complies with the operating protocol of general ADCP surveys on rivers (e.g., RD Instruments, 1999;
660 Simpson, 2002; Mueller and Wagner, 2013). Hence, the developed image-based measurement can be carried out
661 together with the conventional boat-mounted ADCP measurements, further highlighting its time efficiency.
662 Hence, the method offers an alternative approach for assessing riverbed material on-the-go, in underwater
663 circumstances. As an extensive and quick mapping tool, it can support other types of bed material samplings in
664 choosing the sampling locations and their optimal number. Furthermore, it can be used for quickly detecting areas
665 of sedimentation and their extent, as it was shown in Section 3.2. (e.g., Fig. 12b). This way, it can support decision-
666 making regarding the maintenance of the channel or the bank-infiltrated drinking water production (detecting
667 colmation zones). Fourth, a novel approach was used for the imaging and model training. As the camera-bed
668 distance was constantly changing, the mm/pixel ratio also varied. Hence, no scale was defined for the algorithm
669 beforehand. Earlier Deep Learning methods for sediment analysis all applied fixed camera heights and/or provided
670 scaling for the AI. Furthermore, these studies were based on airborne measurements, mapping the dry zone of the
671 rivers. In an underwater manner, it is extremely challenging to keep a fixed, constant camera height due to the
672 spatially varying riverbed elevations. Hence, it is of major importance that this manuscript introduces a
673 methodology and a Deep Learning algorithm which neglect the need for scaling. This way, the method is faster
674 and easier to build, but also simpler to use. Due to this, the method does not reconstruct detailed grainsize
675 distributions, but rather measures the relative portions of the main sediment classes: sand, gravel, cobble. In short,
676 this study showcased a fast bed material mapping tool, with a much denser spatial resolution than the conventional
677 methods, saving up significant resources.

678
679 Originally, beside the three classes of main sediment types introduced in the manuscript, others were also defined
680 during annotation (e.g., bedrock, clams), but due to class imbalance (i.e., dominance of the three sediment classes),
681 these were not adapted successfully. In the future, improving the method through transfer learning (Zamir et al.,
682 2018) using broader dataset and involving other sediment types will be considered. Another option for developing
683 the method is to counter imbalance with the use of so-called weighted cross entropy (see Lu et al., 2019) on the
684 current dataset, which will also be investigated.

685

686 Since the introduced method offers a quick way to provide extensive, spatially dense bed material information of
687 its composition, it can be used to boost the training dataset of predictive, ensemble bagging-based Machine
688 Learning techniques (e.g., Ren et al., 2020) and improve their accuracy. Furthermore, the method can support the
689 implementation of other imagery techniques. For instance, using one of the training videos of this study the authors
690 managed to reconstruct the grain-scale 3D model of a riverbed section with the Structure-from-Motion technique
691 (Ermilov et al., 2020), enabling the quantitative estimation of surface roughness. Underwater field cameras can
692 also be used for monitoring and estimating bedload transport rate (Ermilov et al., 2022) by adapting LS-PIV and
693 the Statistical Background Model approach. This latter videography technique may also be used with moving
694 cameras (e.g., Hayman and Ekhlund, 2003), which enables its adaptation into our method by e.g., detecting
695 bedload movement in the cross-section.

696

697 The statistical representativity of the introduced method, as a surface sampling technique, needs to also be
698 addressed in future work. Following and building upon the experience of conventional, surface sampling
699 procedures (e.g., grid sampling; Diplas, 1988) may prove to be beneficial, where they provided the exact number
700 of gravel particles needed to be included (Wolman, 1954) to satisfy the representativity criteria. Then, using edge-
701 and blob-detection would enable to calculate and compare the number of gravel particles in the images to this
702 value. Furthermore, we intend to apply 2 cameras, with overlapping FOVs for increasing the covered area (and
703 the representativity) during surveys. Besides, it would also improve the accuracy of the Structure-from-Motion
704 technique mentioned earlier.

705 **4 Conclusion**

706 A novel, artificial intelligence-based riverbed sediment analysis method has been introduced in this manuscript,
707 which uses underwater images to reconstruct the spatial variation of the characteristic sediment classes. The
708 method was trained and validated with a reasonably high number (~15000) of images, collected in a large river,
709 in the Hungarian section of the Danube. The main novelties of the developed Deep Learning based procedure are
710 the followings: i) underwater images are used, ii) the method enables mapping of the riverbed along the
711 measurement vessel's route with very dense spatial allocation, iii) cost-efficient, iv) works without scaling, i.e.,
712 the distance between the camera and the riverbed can vary. Consequently, in contrast with conventional pointwise
713 bed sediment analysis methods, this technique is robust and capable of providing continuous sediment
714 composition data covering whole river reaches, eventually providing the possibility to set up 2D bed material
715 maps. In this way, river reach scale hydromorphological assessments can be supported, where the composition of
716 bed surface is of interest, e.g., when performing habitat studies, parameterising 2D and 3D computational
717 hydrodynamic and morphodynamic models, or assessing the impact of restoration measures.

718 **Financial support.** The first author acknowledges the support of the ÚNKP-21-3 New National Excellence
719 Programme of the Ministry for Innovation and Technology, and the National Research, Development and
720 Innovation Fund, Hungary.

721 **Code availability.** The code written and used in this manuscript is available [here](#).

722 **Data availability.** The dataset and results can be accessed using the following links:
723 [link1](#); [link2](#); [link3](#).

724 **Author contributions.** GB developed the code and carried out the training process. AAE carried out the
725 fieldwork, evaluated the results, did the laboratory analysis, and collaborated with GB in improving the images.
726 SB oversaw and directed the project, while managing the financial- and equipment background.

727 **Competing interest.** The contact author has declared that none of the authors has any competing interest.

728 **Acknowledgements.** The authors would like to thank our students Dávid Koós, Gergely Tikász, Schrott Márton
729 and our technicians István Galgóczy, István Pozsgai, Károly Tóth and András ReháK for fieldwork support.

730 **References**

731 Adams, J.: Gravel Size Analysis from Photographs. *J. Hydraul. Div.*, 1979, 105, 1247–1255.
732 doi/10.1061/JYCEAJ.0005283, 1979.

733
734 Anglin, D. R., Haeseker, S. L., Skalicky, J. J., Schaller, H., Tiffan, K. F., Hatten, J. R., et al.: Effects of Hydropower
735 Operations on Spawning Habitat, Rearing Habitat, and Standing/Entrapment Mortality of Fall Chinook Salmon
736 in the Hanford Reach of the Columbia River. US Fish and Wildlife Service, final Report. Available at:
737 <https://pubs.er.usgs.gov/publication/70179516>, 2006.

738
739 Baranya, S., Fleit, G., Józsa, J., Szalóky, Z., Tóth, B., Czeplédi, I. and Erős, T.: Habitat mapping of riverine fish
740 by means of hydromorphological tools. *Ecohydrology*, Volume 11, Issue 7 e2009. Available at:
741 <https://doi.org/10.1002/eco.2009>, 2018.

742
743 Barnard, P., Rubin, D., Harney, J. and Mustain, N.: Field test comparison of an autocorrelation technique for
744 determining grain size using a digital beachball camera versus traditional methods. *Sedimentary Geology*, 201(1–
745 2): 180–195., 2007.

746
747 Benjankar, R., Tonina, D., Mckean, J.: One-dimensional and two-dimensional hydrodynamic modelling derived
748 flow properties: Impacts on aquatic habitat quality predictions. *Earth Surf. Process. Landf.* 2015, 40, 340–356.

749
750 Benkő, G., Baranya, S., Török, T. G., and Molnár, B.: Folyami mederanyag szemösszetételének vizsgálata Mély
751 Tanulás eljárással drónfelvételek alapján (in English: Analysis of composition of riverbed material with Deep
752 Learning based on drone video footages). *Hidrológiai Közölny*, 100, 61–69., 2020. Manuscript
753 Breheret, A.: Pixel Annotation Tool. Av. at: <https://github.com/abreheret/PixelAnnotationTool>, 2017.

754
755 Bunte, K. and Abt, S. R.: Sampling Surface and Subsurface Particle-Size Distributions in Wadable Gravel- and
756 Cobble-Bed Streams for Analyses in Sediment Transport, Hydraulics, and Streambed Monitoring; General
757 Technical Report (GTR), U.S. Department of Agriculture, Forest Service, Rocky Mountain Research Station: Fort
758 Collins, CO, USA, 2001.

759
760
761 Buscombe, D. and Masselink, G.: Grain size information from the statistical properties of digital images of
762 sediment. *Sedimentology*, 56, 421–438. doi/10.1111/j.1365-3091.2008.00977.x, 2008.

763
764 Buscombe, D.: Transferable wavelet method for grain-size distribution from images of sediment surfaces and thin
765 sections, and other natural granular patterns. *Sedimentology*, 60 1709–1732., 2013.

766
767 Buscombe, D., Grams, P. and Kaplinski, M.: Characterizing riverbed sediment using high-frequency acoustics: 1.
768 Spectral properties of scattering. *Journal of Geophysical Research: Earth Surface*, doi: 10.1002/2014JF003189,
769 119:12, (2674–2691), 2014a.

770

771 Buscombe, D., Grams, P. and Kaplinski, M.: Characterizing riverbed sediment using high-frequency acoustics: 2.
772 Scattering signatures of Colorado Riverbed sediment in Marble and Grand Canyons. *Journal of Geophysical*
773 *Research: Earth Surface*, doi/full/10.1002/2014JF003191, 119:12, (2674-2691), 2014b.
774
775 Buscombe, D. and Ritchie, A. C.: Landscape Classification with Deep Neural Networks. *Geosciences*, 8, 244.
776 Available at: <https://doi.org/10.3390/geosciences8070244> , 2018.
777
778 Buscombe, D.: SediNet: a configurable deep learning model for mixed qualitative and quantitative optical
779 granulometry optical granulometry. *Earth Surface Processes and Landforms*, 45, 638-651. DOI:
780 10.1002/esp.4760, 2020.
781
782
783 Chandler, J., Lane, S. N. and Ashmore, P.: Measuring river-bed and flume morphology and parameterising bed
784 roughness with a KODAK DCS460 digital camera. *International Archives of Photogrammetry and Remote*
785 *Sensing*, Vol. XXXIII, Part B7., 2000.
786
787 Chen, C., Zhang, P., Zhang, H., Dai, J., Yi, Y., Zhang, H. and Zhang, Y.: Deep Learning on Computational-
788 Resource-Limited Platforms: A Survey. Volume 2020, Article ID 8454327. Available at:
789 <https://doi.org/10.1155/2020/8454327>, 2020.
790
791 Chen, L., Zhu, Y., Isola, P., Papandreou, G., Schroff, F. and Adam, H.: Encoder-Decoder with Atrous Separable
792 Convolution for Semantic Image Segmentation. *Proceedings of the European conference on computer vision*
793 *(ECCV)* (pp. 801-818). <https://arxiv.org/abs/1802.02611>, 2018.
794
795 Cheng, D., Li, X., Li, W. H., Lu, C., Li, F., Zhao, H. and Zheng, W. S.: Large-Scale Visible Watermark Detection
796 and Removal with Deep Convolutional Networks. In book: *Pattern Recognition and Computer Vision. First*
797 *Chinese Conference, PRCV, Guangzhou, China, Proceedings, Part III*. DOI: 10.1007/978-3-030-03338-5_3,
798 2018.
799
800 Cheng, Z., and Liu, H.: Digital grain-size analysis based on autocorrelation algorithm. *Sedimentary Geology*, 327,
801 21-31. Available at: <https://doi.org/10.1016/j.sedgeo.2015.07.008>, 2015.
802
803 Chezar, H. and Rubin, D. M.: Underwater Microscope System. United States Patent Office, The United States of
804 America as represented by the Secretary of the Interior, US Patent No. 6,680,795 B2., 2004.
805
806 Church, M. A., McLean, D. G., and Wolcott, J. F.: Sediments transport in Gravel Bed Rivers. Chap.: *Riverbed*
807 *Gravels: Sampling and Analysis*. John Wiley and Sons, New York, 43–88, 1987.
808
809 Cui, G., Su, X., Liu, Y., & Zheng, S.: Effect of riverbed sediment flushing and clogging on river-water infiltration
810 rate: a case study in the Second Songhua River, Northeast China. *Hydrogeology Journal*, 29(2), 551–565.
811 <https://doi.org/10.1007/s10040-020-02218-7>, 2021.
812
813 Delong, M. D. and Brusven, M. A.: Classification and spatial mapping of riparian habitat with applications toward
814 management of streams impacted by nonpoint source pollution. *Environmental Management*, 15:565-571. DOI:
815 10.1007/BF02394745, 1991.
816
817 Detert, M. and Weitbrecht, V.: User guide to gravelometric image analysis by BASEGRAIN. In *Advances in*
818 *Science and Research*; Fukuoka, S., Nakagawa, H., Sumi, T., Zhang, H., Eds.; Taylor and Francis Group: London,
819 UK, 2013; pp. 1789–1795. ISBN 978-1-138-00062-9., 2013.
820
821 Diplas, P.: Sampling Techniques for Gravel Sized Sediments. *Journal of Hydraulic Engineering*. DOI:
822 10.1061/(ASCE)0733-9429(1988)114:5(484), 1988.
823
824 Ermilov, A.A., Baranya, S. and Török, G.T.: Image-Based Bed Material Mapping of a Large River. *Water*, 12,
825 916. Available at: <https://doi.org/10.3390/w12030916>, 2020.
826
827 Ermilov, A. A., Fleit, G., Conevski, S., Guerrero, M., Baranya, S., & Rütther, N.: Bedload transport analysis using
828 image processing techniques. *ACTA GEOPHYSICA*, 1895-6572 1895-7455. [http://doi.org/10.1007/s11600-022-](http://doi.org/10.1007/s11600-022-00791-x)
829 [00791-x](http://doi.org/10.1007/s11600-022-00791-x), 2022.
830

831 Fehr, R.: Einfache Bestimmung der Korngrößenverteilung von Geschiebematerial mit Hilfe der
832 Linienzahlanalyse (In English: Simple detection of grain size distribution of sediment material using line-count
833 analysis). Schweizer Ing. und Archit., 105, 1104–1109., 1987.

834

835 Ferdowski, B., Ortiz, C. P., Houssais, M., & Jerolmack, D. J. (2017). Riverbed armouring as a granular segregation
836 phenomenon. Nature Communications 2017 8:1, 8(1), 1–10. <https://doi.org/10.1038/s41467-017-01681-3>

837

838 Fetzer, J., Holzner, M., Plötze, M. and Furrer, G.: Clogging of an Alpine streambed by silt-sized particles –
839 Insights from laboratory and field experiments. Water Research, Volume 126, Pages 60-69.
840 <https://doi.org/10.1016/j.watres.2017.09.015>, 2017.

841

842 Geist, D. R., Jones, J., Murray, C. J. and Dauble, D. D.: Suitability criteria analyzed at the spatial scale of redd
843 clusters improved estimates of fall chinook salmon (*Oncorhynchus tshawytscha*) spawning habitat use in the
844 Hanford Reach, Columbia River. Canadian Journal of Fisheries and Aquatic Sciences, 57: 1636-1646., 2000.

845

846 Gilcher, M. and Udelhoven, T.: Field Geometry and the Spatial and Temporal Generalization of Crop
847 Classification Algorithms—A Randomized Approach to Compare Pixel Based and Convolution Based Methods.
848 Remote Sens., 13, 775., 2021.

849

850 GOPRO Hero 4 Silver: User Manual. Available at: [https://gopro.com/content/dam/help/hero4-](https://gopro.com/content/dam/help/hero4-silver/manuals/UM_H4Silver_ENG_REVA_WEB.pdf)
851 [silver/manuals/UM_H4Silver_ENG_REVA_WEB.pdf](https://gopro.com/content/dam/help/hero4-silver/manuals/UM_H4Silver_ENG_REVA_WEB.pdf), 2014.

852

853 GOPRO Hero 7 Black: User Manual. Available at: [https://gopro.com/content/dam/help/hero7-](https://gopro.com/content/dam/help/hero7-black/manuals/HERO7Black_UM_ENG_REVA.pdf)
854 [black/manuals/HERO7Black_UM_ENG_REVA.pdf](https://gopro.com/content/dam/help/hero7-black/manuals/HERO7Black_UM_ENG_REVA.pdf), 2018.

855

856 Graham, D. J., Reid, I. and Rice, S. P.: Automated sizing of coarse-grained sediments: image-processing
857 procedures. Mathematical Geology, 37, 1–28. <https://doi.org/10.1007/s11004-005-8745-x>, 2005.

858

859 Graham, D. J. Rollet, A.J., Piégay, H. and Rice, S. P.: Maximizing the accuracy of image-based surface sediment
860 sampling techniques. Water Resour. Res., 46, W02508. [https://doi.org/](https://doi.org/10.1029/2008WR006940)
861 [10.1029/2008WR006940](https://doi.org/10.1029/2008WR006940), 2010.

862

863 Grams, P. E., Topping, D. J., Schmidt, J. C., Hazel, J. E. and Kaplinski, M.: Linking morphodynamic response
864 with sediment mass balance on the Colorado River in Marble Canyon: Issues of scale, geomorphic setting, and
865 sampling design, J. Geophys. Res. Earth Surf., 118, 361–381, doi:10.1002/jgrf.20050., 2013.

866

867 Guerit, L., Barrier, L., Liu, Y., Narteau, C., Lajeunesse, E., Gayer, E., Métivier, F.: Uniform grain-size distribution
868 in the active layer of a shallow, gravel-bedded, braided river (the Urumqi River, China) and implications for paleo-
869 hydrology. Earth Surface Dynamics. 6. 1011-1021. DOI: 10.5194/esurf-6-1011-2018., 2018.

870

871 Guerrero, M., Rüther, N., Szupiany, R., Haun, S., Baranya, S. and Latosinski, F.: The Acoustic Properties of
872 Suspended Sediment in Large Rivers: Consequences on ADCP Methods Applicability. Water, 8, 13;
873 doi:10.3390/w8010013, 2016.

874

875 Haddadchi, A., Booker, D.J. and Measures, R.J.: Predicting riverbed substrate cover proportions across New
876 Zealand. Catena, Volume 163, pp. 130-146. Available at: <https://doi.org/10.1016/j.catena.2017.12.014>, 2018.

877

878 Hayman, E., Eklundh, J.: Statistical Background Subtraction for a Mobile Observer. Proceedings of the Ninth
879 IEEE International Conference on Computer Vision (ICCV 2003) 2-Volume Set 0–7695–1950–4/03, 2003.

880

881 He, F., Liu, T., Tao, D.: Control batch size and learning rate to generalize well: theoretical and empirical evidence.
882 Neural Information Processing Systems, 2019.

883

884 Ibbeken, H., and Schleyer, R.: Photo-sieving: A method for grain-size analysis of coarse-grained, unconsolidated
885 bedding surfaces. Earth Surf. Process. Landforms, 11, 59–77. Available at:
886 <https://doi.org/10.1002/esp.3290110108>, 1986.

887

888 Ighathinathane, C., Melin, S., Sokhansanj, S., Bi, X., Lim, C. J., Pordesimo, L. O. and Columbus, E. P.: Machine
889 vision based particle size and size distribution determination of airborne dust particles of wood and bark pellets.
890 Powder Technol., 196, 202–212. Available at: <https://doi.org/10.1016/j.powtec.2009.07.024>, 2009.

891
892 Kellerhals, R. and Bray, D. I.: Sampling Procedures for Coarse Fluvial Sediments. *J. Hydraul. Div.*, 97, 1165–
893 1180., 1971.
894
895 Kim, H., Han, J. and Han, T. Y.: Machine vision-driven automatic recognition of particle size and morphology in
896 SEM images. *Nanoscale*, 12, 19461–19469. Available at: <https://doi.org/10.1039/D0NR04140H>, 2020.
897
898 Kinsman, N.: Single-Beam Bathymetry Data Collected in Shallow-Water Areas near Gambell, Golovin, Hooper
899 Bay, Savoonga, Shishmaref, and Wales, Alaska 2012–2013; Department of Natural Resources. Division of
900 Geological & Geophysical Surveys: Fairbanks, AK, USA, 2015.
901
902 Le, Q. V.: Building high-level features using large scale unsupervised learning. In Proceedings of the 2013 IEEE
903 International Conference on Acoustics, Speech and Signal Processing, Vancouver, BC, Canada, pp. 8595–8598.,
904 2013.
905
906 Leopold, L. B.: An Improved Method for Size Distribution of Stream Bed Gravel. *Water Resour. Res.*, 6, 1357–
907 1366. <https://doi.org/10.1029/WR006i005p01357>, 1970.
908
909 Limare, A., Tal, M., Reitz, M. D., Lajeunesse, E., and Métivier, F.: Optical method for measuring bed topography
910 and flow depth in an experimental flume. *Solid Earth*, 2, 143–154, <https://doi.org/10.5194/se-2-143-2011>., 2011.
911
912 Lowe, D. G.: Distinctive Image Features from Scale-Invariant Keypoints. *International Journal of Computer*
913 *Vision*, 60, pages 91–110, 2004.
914
915 Lu, S., Gao, F., Piao, Ch. and Ma, Y.: Dynamic Weighted Cross Entropy for Semantic Segmentation with
916 Extremely Imbalanced Data. 2019 International Conference on Artificial Intelligence and Advanced
917 Manufacturing (AIAM). doi: 10.1109/AIAM48774.2019.00053, 2019.
918
919 Mueller D. S., Wagner, Ch. R.: Measuring Discharge with Acoustic Doppler Current Profilers from a Moving
920 Boat. USGS, Chapter 22 of Book 3, Section A. <https://pubs.usgs.gov/tm/3a22/>, 2009.
921
922 Muñoz-Mas, R., Sánchez-Hernández, J., McClain, M. E., Tamatamah, R., Mukama, S. C., & Martínez-Capel, F.:
923 Investigating the influence of habitat structure and hydraulics on tropical macroinvertebrate communities.
924 *Ecohydrology and Hydrobiology*, 19(3), 339–350. <https://doi.org/10.1016/j.ecohyd.2018.07.005>, 2019.
925
926 Mueller D. S., Wagner, Ch. R.: Measuring discharge with acoustic Doppler current profilers from a moving boat,
927 version 2.0. [https://www.researchgate.net/publication/284587353_Measuring_discharge_with_acoustic_-_](https://www.researchgate.net/publication/284587353_Measuring_discharge_with_acoustic_-_Doppler_current_profilers_from_a_moving_boat)
928 [Doppler current profilers from a moving boat](https://www.researchgate.net/publication/284587353_Measuring_discharge_with_acoustic_-_Doppler_current_profilers_from_a_moving_boat), 2013.
929
930 Muste, M., Baranya, S., Tsubaki, R., Kim, D., Ho, H., Tsai, H. and Law, D.: Acoustic mapping velocimetry. *Water*
931 *Resour. Res.*, 52, 4132–4150, doi:10.1002/2015WR018354., 2016.
932
933 Obodovskiy, O., Habel, M., Szatten, D., Rozlach, Z., Babiński, Z., Maerker, M.: Assessment of the Dnieper
934 Alluvial Riverbed Stability Affected by Intervention Discharge Downstream of Kaniv Dam. *Water*, 12(4):1104.
935 <https://doi.org/10.3390/w12041104>, 2020.
936
937 Padilla, R., Netto, S. M. and da Silva, E. A. B.: A Survey on Performance Metrics for Object-Detection
938 Algorithms. Conference: 2020 International Conference on Systems, Signals and Image Processing (IWSSIP).
939 DOI: 10.1109/IWSSIP48289.2020, 2020.
940
941 Perez, L. and Wang, J.: The Effectiveness of Data Augmentation in Image Classification using Deep Learning.
942 arXiv preprint arXiv:1712.04621. Av. at: <https://arxiv.org/abs/1712.04621>. 2017., 2017.
943
944 Purinton, B. and Bookhagen, B.: Introducing PebbleCounts: A grain-sizing tool for photo surveys of dynamic
945 gravel-bed rivers. *Earth Surf. Dyn.*, 7, 859–877. <https://doi.org/10.5194/esurf-7-859-2019>, 2019.
946
947 Rákóczi, L.: Selective erosion of noncohesive bed materials. *Geografiska Annaler. Series A, Physical Geography*,
948 Vol. 69, No. 1, pp. 29-35. <https://doi.org/10.2307/521364>, 1987.
949

950 Rákóczi, L.: Identification of river channel areas inclined for colmation, based on the analysis of bed material.
951 *Vízügyi Közlemények*, LXXIX., chapter 3., 1997.
952

953 Rahman, M. A. and Wang, Y.: Optimizing Intersection-Over-Union in Deep Neural Networks for Image
954 Segmentation. In: Bebis G. et al. (eds) *Advances in Visual Computing. ISVC 2016. Lecture Notes in Computer
955 Science*, vol 10072. Springer, Cham. https://doi.org/10.1007/978-3-319-50835-1_22, 2016.
956

957 RD Instruments – Acoustic Doppler Current Profilers – Application Note: https://www.commtec.com/library/Technical_Manuscripts/RDI/FSA-004%20Mode1.pdf, 1999.
958
959

960 Rice, S. and Church, M.: Grain size along two gravel-bed rivers: Statistical variation, spatial pattern and
961 sedimentary links. *Earth Surf. Process. Landf.*, 23, 345–363., 1998.
962

963 Ren, H., Hou, Z., Duan, Z., Song, X., Perkins, W.A., Richmond, M. C., Arntzen, E. V. and Scheibe, T. D.: Spatial
964 Mapping of Riverbed Grain-Size Distribution Using Machine Learning. *Front. Water*, 2:551627. doi:
965 10.3389/frwa.2020.551627, 2020.
966

967 Rozniak, A., Schindler, K., Wegner, J. D. and Lang, N.: Drone images and Deep Learning for river monitoring in
968 Switzerland. Semester project. Institute of Geodesy and Photogrammetry, Project, Swiss Federal Institute of
969 Technology (ETH) Zurich, 2019.
970

971 Rubin, D. M.: A simple autocorrelation algorithm for determining grain-size from digital images of sediment. *J.
972 Sed. Res.*, 74, 160–165., 2004.
973

974 Rubin, D. M., Chezar, H., Harney, J. N., Topping, D. J., Melis, T. S., Sherwood, C. R.: Underwater microscope
975 for measuring spatial and temporal changes in bed-sediment grain size. *Sedimentary Geology*, Volume 202, Issue
976 3, Pages 402-408, <https://doi.org/10.1016/j.sedgeo.2007.03.020>, 2007.
977

978 Scheder, C., Lerchegger, B., Flödl, P., Csar, D., Gumpinger, C. and Hauer, C.: Riverbed stability versus clogged
979 interstitial: Depth-dependent accumulation of substances in freshwater pearl mussel (*Margaritifera margaritifera*
980 L.) habitats in Austrian streams as a function of hydromorphological parameters. *Limnologica*, Volume 50,
981 January 2015, Pages 29-39. <https://doi.org/10.1016/j.limno.2014.08.003>, 2015.
982

983 Shields, F. D., Jr. and Rigby, J. R.: River habitat quality from river velocities measured using acoustic Doppler
984 current profiler. *Environ. Manage.*; 36(4):565-75. doi: 10.1007/s00267-004-0292-6., 2005.
985

986 Shields, F. D. Jr.: Aquatic Habitat Bottom Classification Using ADCP. *Journal of Hydraulic Engineering*, Vol.
987 136, Issue 5, 2010.
988

989 Sime, L. C. and Ferguson, R. I.: Information on grain-sizes in gravel bed rivers by automated image analysis. *J.
990 Sed. Res.*, 73, 630–636., 2003.
991

992 Simpson, M. R.: Discharge Measurements Using a Broad-Band Acoustic Doppler Current Profiler. USGS, Open-
993 File Report 01-1, <https://pubs.usgs.gov/of/2001/ofr0101/>, 2002.
994

995 Singer, M. B.: A new sampler for extracting bed material sediment from sand and gravel beds in navigable rivers.
996 *Earth Surface Processes and Landforms* 33(14):2277 – 2284 DOI: 10.1002/esp.1661, 2008.
997

998 Soloy, A., Turki, I., Fournier, M., Costa, S., Peuziat, B. and Lecoq, N.: A Deep Learning-Based Method for
999 Quantifying and Mapping the Grain Size on Pebble Beaches. *Remote Sens.*, 12, 3659, doi:10.3390/rs12213659,
1000 2020.
1001

1002 Staudt, F., Mullarney, J. C., Pilditch, C. A. and Huhn, K.: Effects of grain-size distribution and shape on sediment
1003 bed stability, near-bed flow and bed microstructure. *Earth Surface Processes and Landforms*, 44(5). DOI:
1004 10.1002/esp.4559, 2018.
1005

1006 Sun, Z., Zheng, H. and Sun, L.: Analysis on the Characteristics of Bed Materials in the Jinghong Reservoir on the
1007 Lancang River. *Sustainability*, 13, 6874. <https://doi.org/10.3390/su13126874>, 2021.
1008

1009 Takechi, H., Aragaki, S. and Irie, M.: Differentiation of River Sediments Fractions in UAV Aerial Images by
1010 Convolution Neural Network. *Remote Sens.*, 13, 3188. <https://doi.org/10.3390/rs13163188>, 2021.

1011

1012 Taravat, A., Wagner, M. P., Bonifacio, R. and Petit, D.: Advanced Fully Convolutional Networks for Agricultural
1013 Field Boundary Detection. *Remote Sens.*, 13, 722., 2021.

1014

1015 Török, G. T., Baranya, S. (2017) Morphological Investigation of a Critical Reach of the Upper Hungarian Danube.
1016 *Periodica Polytechnica Civil Engineering*. 61(4), pp. 752–761. <https://doi.org/10.3311/PPci.10530>, 2017.

1017

1018 USDA: Guidelines for Sampling Bed Material. Technical Supplement 13A, 2007.

1019

1020 Vanoni, V. A. and Hwang, L. S.: Relation between Bed Forms and Friction in Streams. *J. Hydraulics Division.*,
1021 93 (3), 121–144. doi:10.1061/JYCEAJ.0001607, 1967.

1022

1023 Verdú, J. M., Batalla, R. J. and Martínez-Casanovas, J. A.: High-resolution grain-size characterisation of gravel
1024 bars using imagery analysis and geo-statistics. *Geomorphology*, 72, 73–93., 2005.

1025

1026 Warrick, J. A., Rubin, D. M., Ruggiero, P., Harney, J. N., Draut, A. E. and Buscombe, D.: Cobble cam: Grain-
1027 size measurements of sand to boulder from digital photographs and autocorrelation analyses. *Earth Surf. Process
1028 Landf.*, 34, 1811–1821. <https://doi.org/10.1002/esp.1877>, 2009.

1029

1030 Wilcock, P. R.: Persistence of armor layers in gravel-bed streams. *Hydrology and Land Surface Studies*.
1031 <https://doi.org/10.1029/2004GL021772>, 2005.

1032

1033 Wolcott, J. F., Church, M.: Strategies for sampling spatially heterogeneous phenomena: The example of river
1034 gravels. *Journal of Sedimentary Research*. v. 61, no. 4, p. 534–543, 1991.

1035

1036 Wolman, M. G.: Method of sampling coarse river bed material. *Trans. Am., Geophysical Union*, 35(6), 951-956.
1037

1038 WMO: Measurement of river sediments: prepared by the Rapporteur on Sediment Transport of the Commission
1039 for Hydrology. Report, World Meteorological Organization - No. 561, Operational hydrology report (OHR)- No.
1040 16, 1981.

1041

1042 Xiao, Y., Li, W., & Yang, S.: Hydrodynamic-sediment transport response to waterway depth in the Three Gorges
1043 Reservoir, China. *Arabian Journal of Geosciences*, 14(775). <https://doi.org/10.1007/s12517-021-07090-7>
1044 /Published, 2021.

1045

1046 Yang, F., Yi, M., Cai, Y., Blasch, E., Sullivan, N., Sheaff, C., Chen, G. and Ling, H.: Multitask Assessment of
1047 Roads and Vehicles Network (MARVN). *Proceedings Volume 10641, Sensors and Systems for Space
1048 Applications XI*, 106410D, <https://doi.org/10.1117/12.2305972>, 2018.

1049

1050 You, K., Long, M., Wang, J., Jordan M.I.: How Does Learning Rate Decay Help Modern Neural Networks?
1051 <https://doi.org/10.48550/arXiv.1908.01878>, 2019.

1052

1053 Yu, L., Wang, S. and Lai, K.K.: Data Preparation in Neural Network Data Analysis. In book: *Foreign-Exchange-
1054 Rate Forecasting with Artificial Neural Networks*. DOI: 10.1007/978-0-387-71720-3_3, 2007.

1055

1056 Zamir, A. R., Sax, A., Shen, W., Guibas, L., Malik, J. and Savarese, S.: Taskonomy: Disentangling Task Transfer
1057 Learning. In *Proceedings of the 2018 IEEE/CVF Conf. on Computer Vision and Pattern Recognition*, Salt Lake
1058 City, UT, USA, pp. 3712–3722. doi: 10.1109/CVPR.2018.00391, 2018.

1059

1060 Zhang, Q., Shi, Y., Chen, Z. and Jiang, T.: ADCP measured flow current of the middle-lower Changjiang River
1061 channel. *Front. Earth Sci., China* 2, 1–9. <https://doi.org/10.1007/s11707-008-0016-y>, 2008.

1062

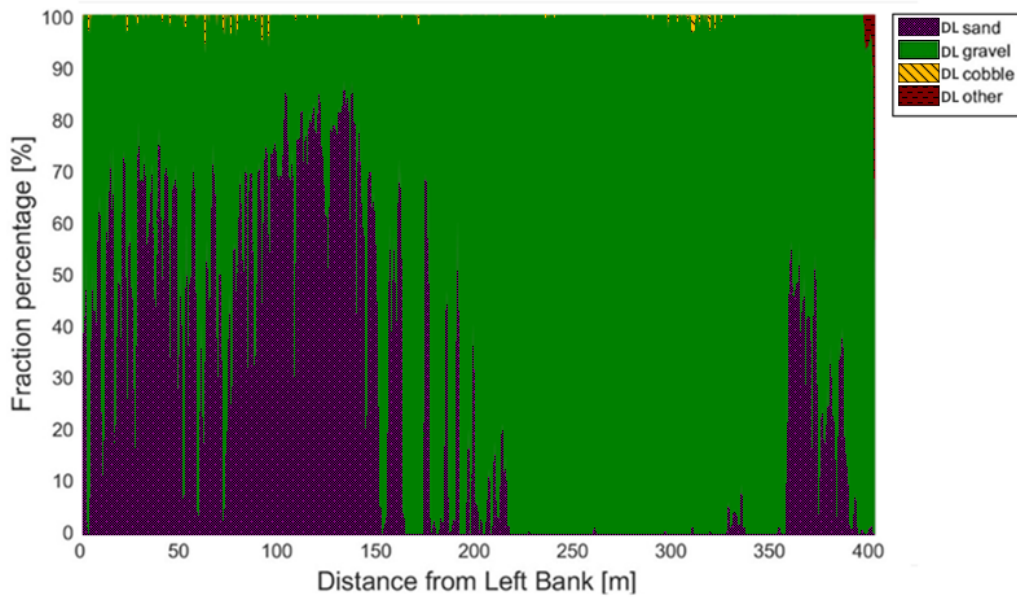
1063 Zhou, Y., Lu, J., Jin, Z., Li, Y., Gao, Y., Liu, Y. and Chen, P.: Experimental Study on the Riverbed Coarsening
1064 Process and Changes in the Flow Structure and Resistance in the Gravel Riverbed Downstream of Dams. *Front.
1065 Environ. Sci.*, <https://doi.org/10.3389/fenvs.2021.611668>, 2021.

1066

1067 Zhu, J., Park, T., Isola, P. and Efros, A. A.: Unpaired Image-to-Image Translation using Cycle-Consistent
1068 Adversarial Networks. arxiv, <https://arxiv.org/abs/1703.10593>, 2020.

1069 Appendix

1070 Appendix A Site A - Section A – II



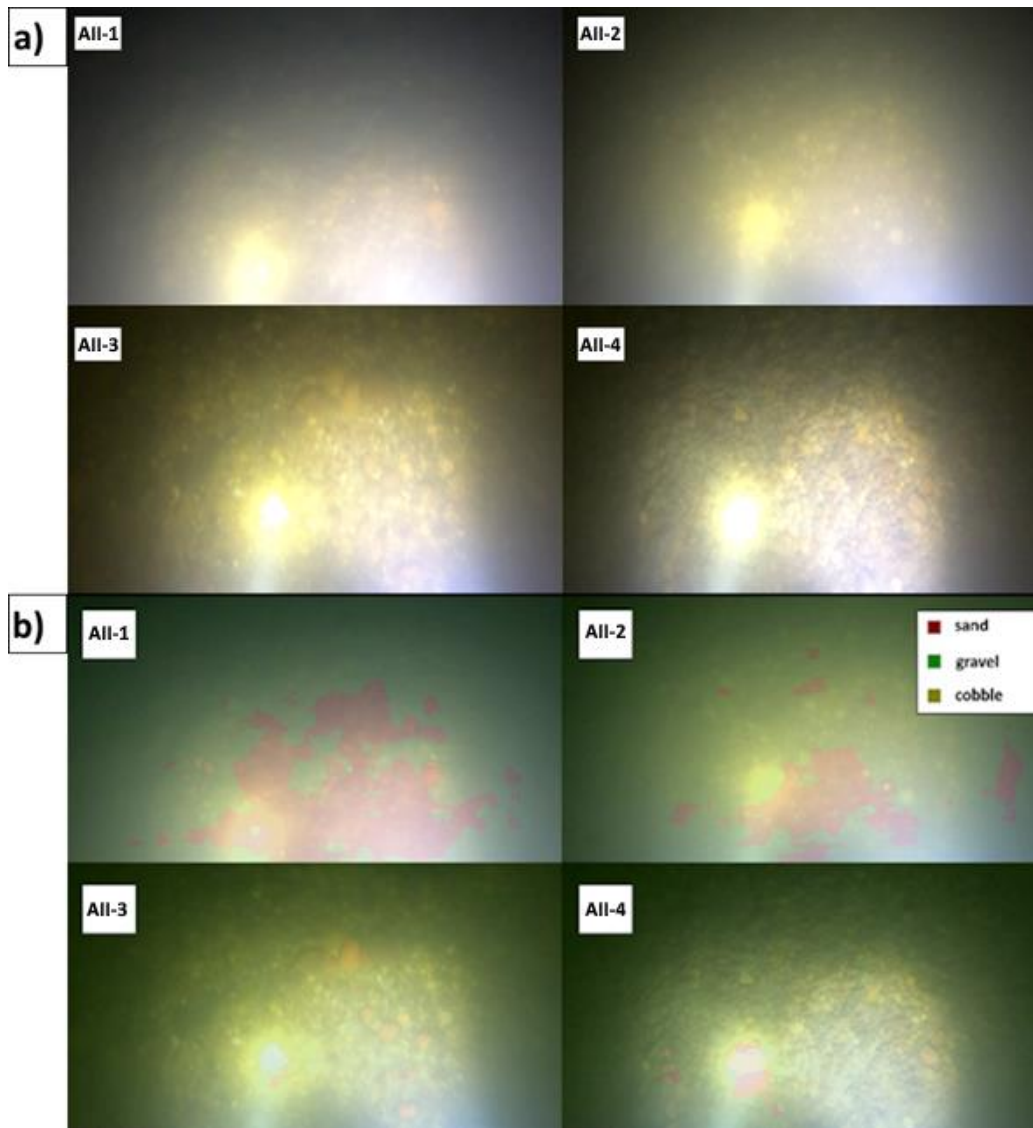
1071 Figure A1: The sediment fraction percentage results of every image, analysed by the DL algorithm along Section A -
1072 II. While the trends are apparent, the sensitivity of the method at its current state can be observed. DL result before
1073 applying moving-averaging.
1074

1075



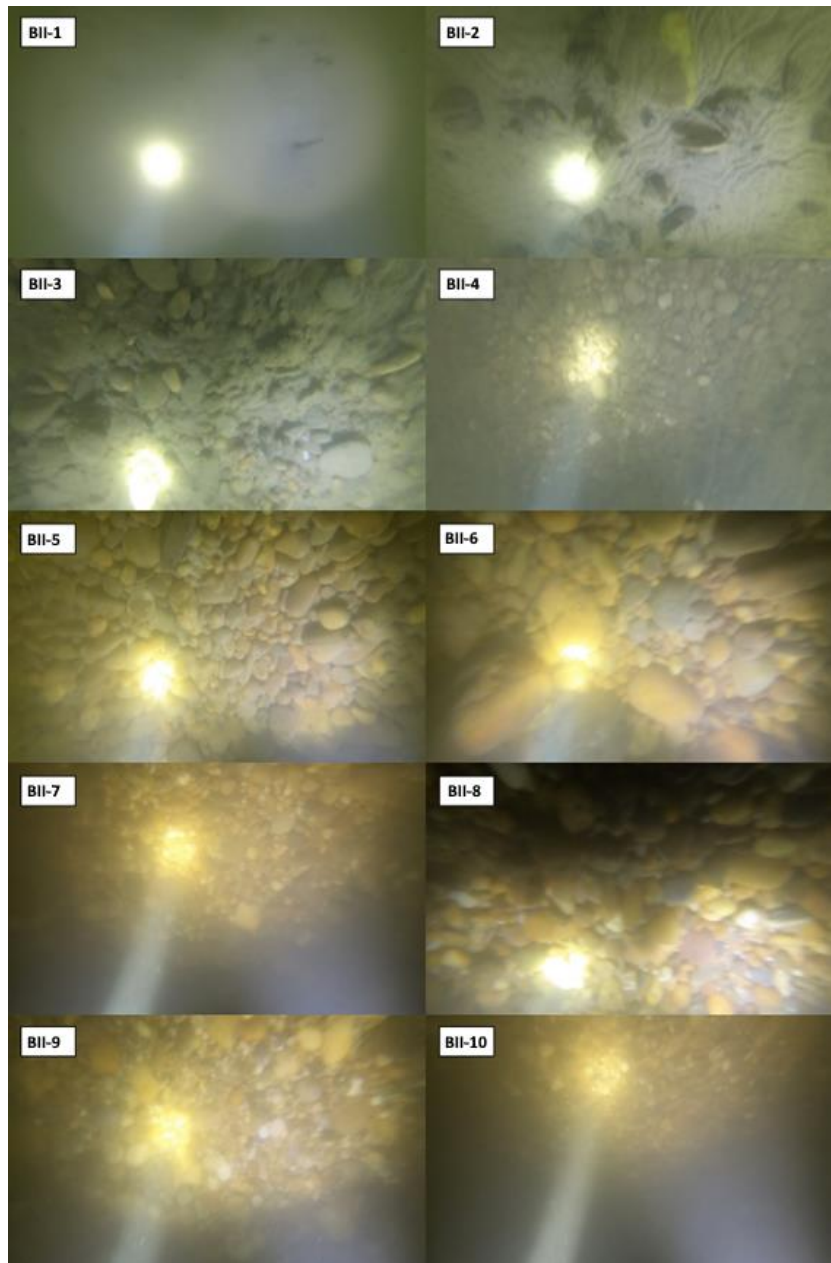
1076 Figure A2: Images of bed armouring, taken during our surveys in the Upper section of the Hungarian Danube. We
1077 broke the surface armour to showcase the presence of the underlying finer fractions.
1078

1079



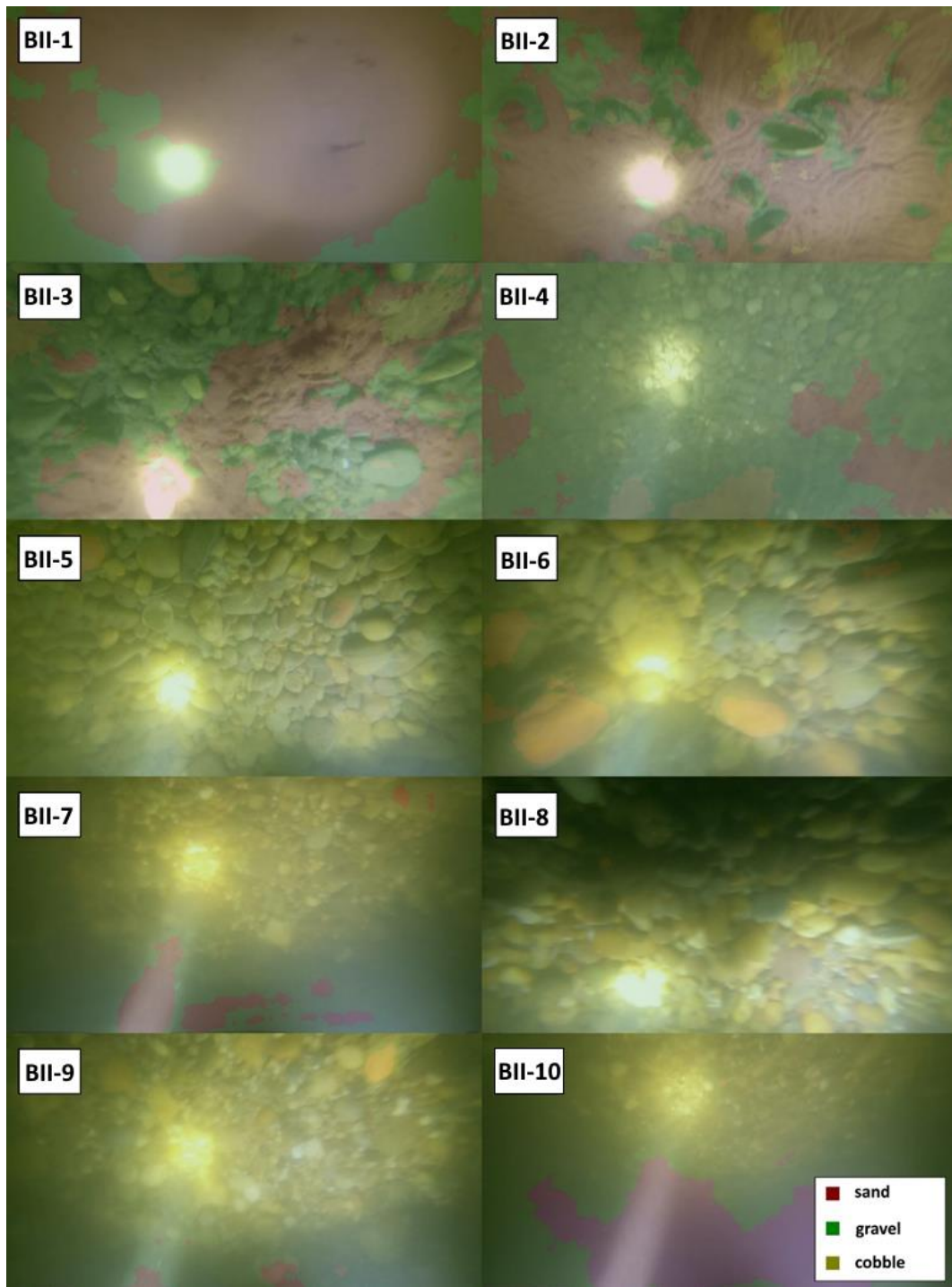
1080
 1081
 1082

Figure A3: a) Riverbed video images at the sampling points in Section A - II. b) Riverbed video images overlapped with their raw, DL detection result, at the sampling points in Section A - II.



1084 Figure B1: Riverbed video images at the sampling points in Section B - II.
1085

1086



1087

1088

1089

Figure B2: Riverbed video images overlapped with their raw, DL detection result, at the sampling points in Section B - II.

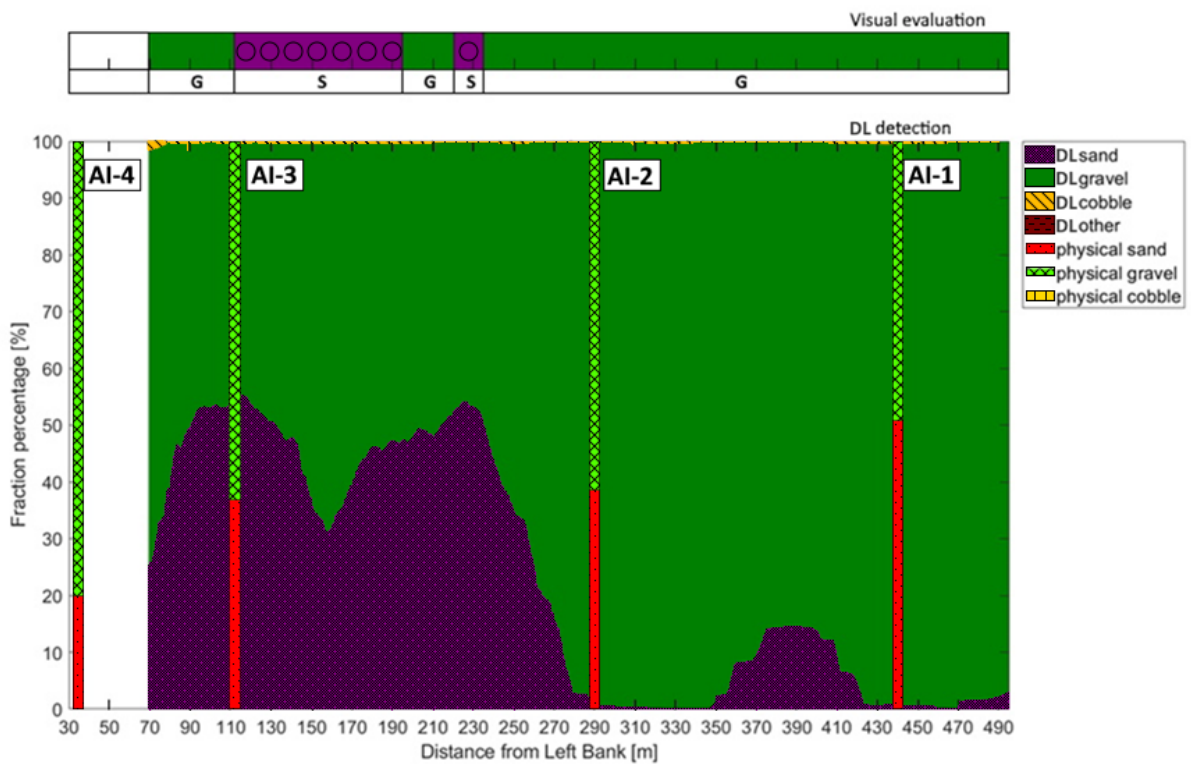
1090

1091 Appendix C Site A - Section A – I



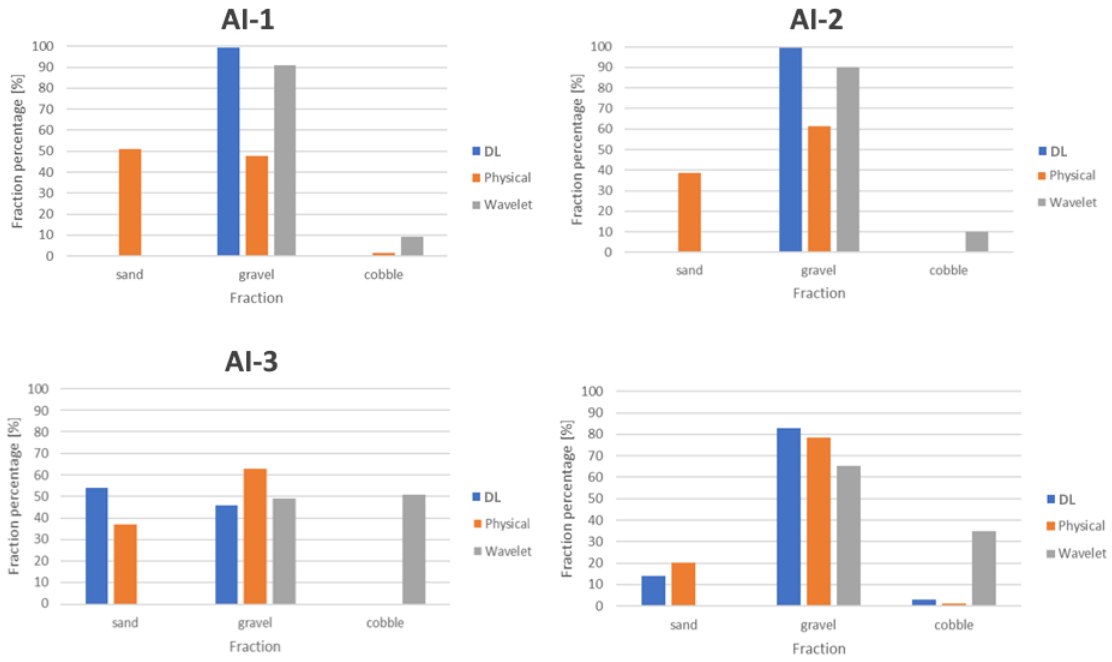
1092 Figure C1: The path of the vessel and camera in Section A - I, Site A. The polyline is coloured based on the sediment
 1093 seen during visual evaluation of the video. Yellow markers are the locations of physical bed material samplings. (Map
 1094 created with Google Earth Pro)
 1095

1096



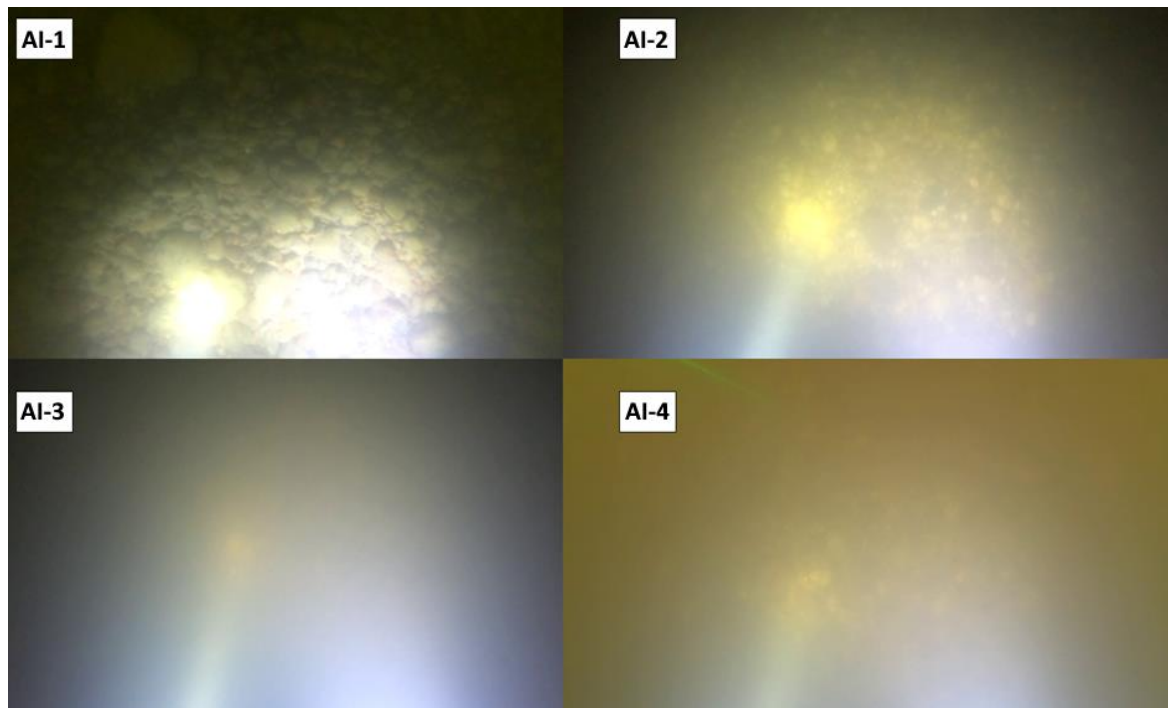
1097 Figure C2: Sediment fraction percentages in Section A - I, recognised by the AI. The visual evaluation included two
 1098 classes: gravel – G, sand – S). The fractions of the physical samples are shown as verticals.
 1099

1100



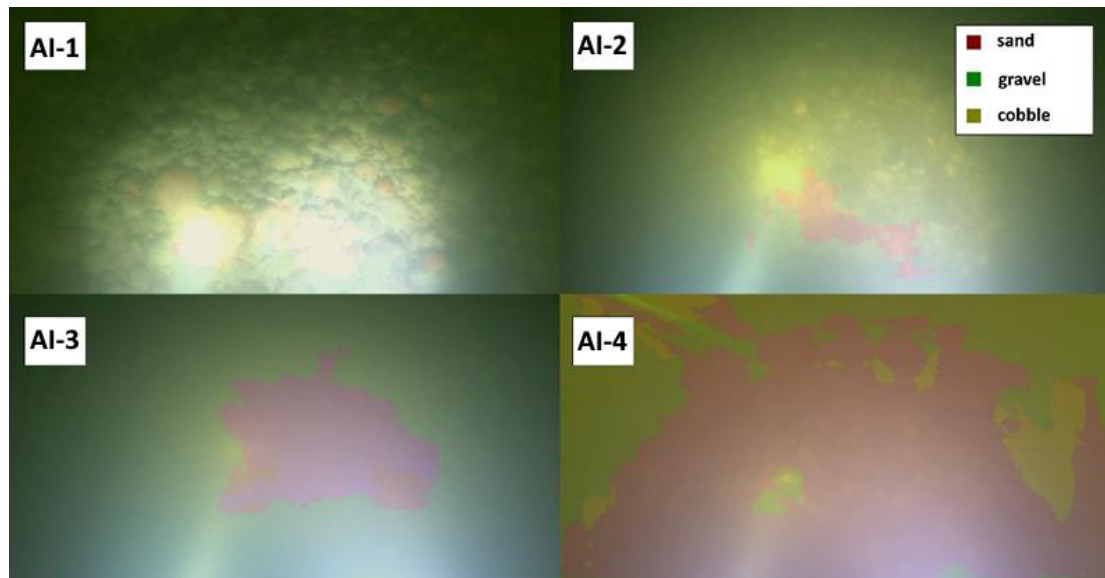
1101
1102
1103

Figure C3: Comparison of sediment fraction % at the sampling locations from the moving-averaged DL detection, conventional sieving and the wavelet-based image processing method. Section A - I.



1104
1105
1106

Figure C4: Riverbed video images at the sampling points in Section A - I.



1107

1108

1109

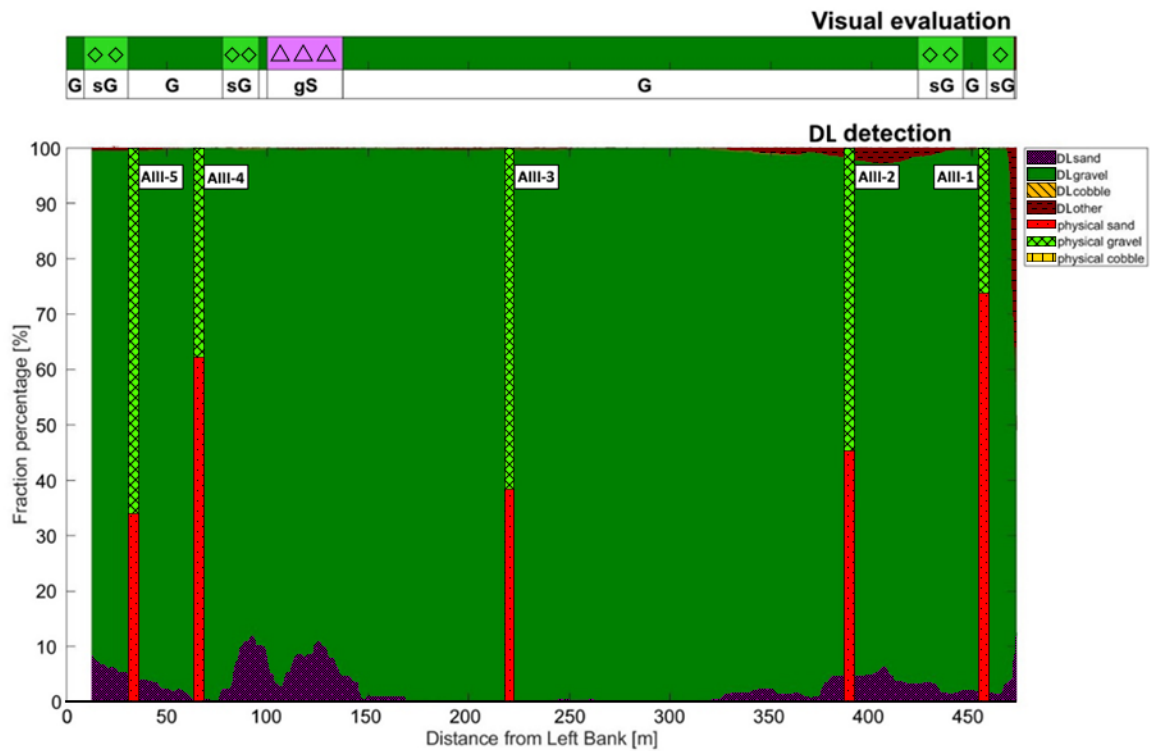
Figure C5: Riverbed video images overlapped with their raw, DL detection result, at the sampling points in Section A-I.

1110 Appendix D Site A – Section A - III

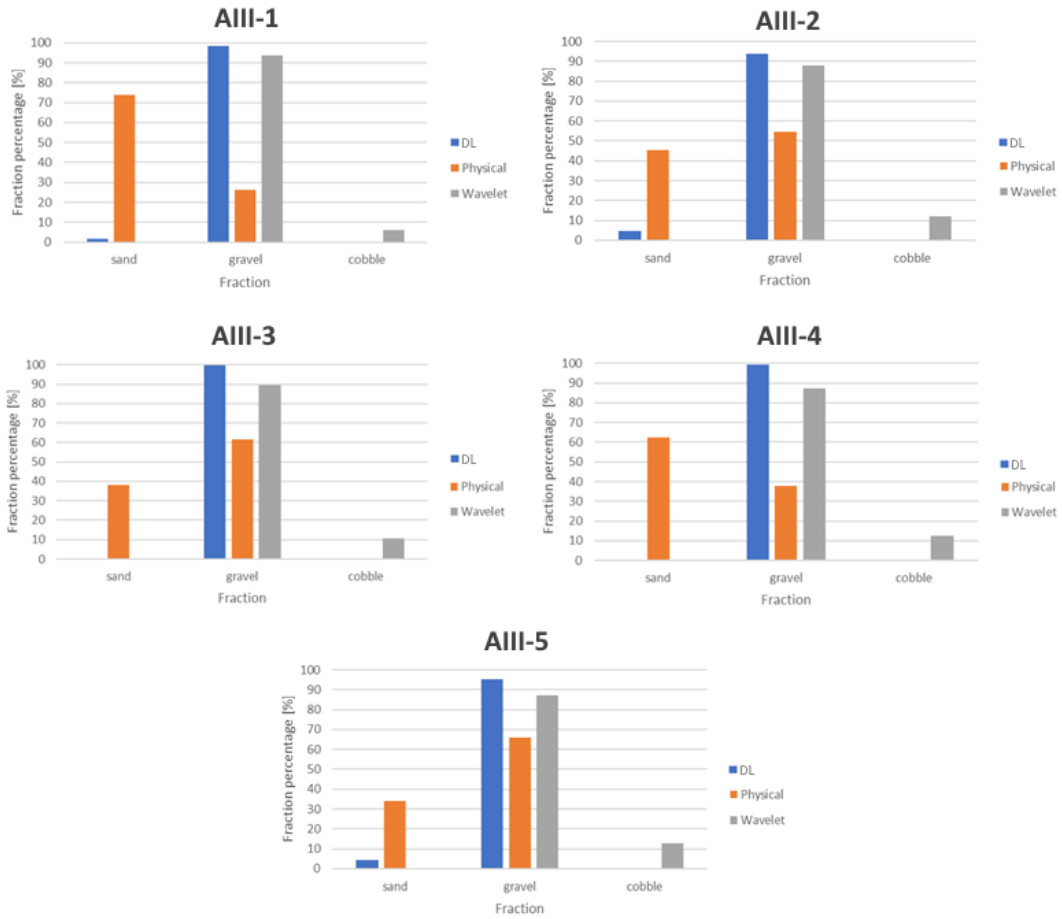


1111 Figure D1: The path of the vessel and camera in Section A - III, Site A. The polyline is coloured based on the sediment
 1112 seen during visual evaluation of the video. Yellow markers are the locations of physical bed material samplings. (Map
 1113 created with Google Earth Pro)
 1114

1115

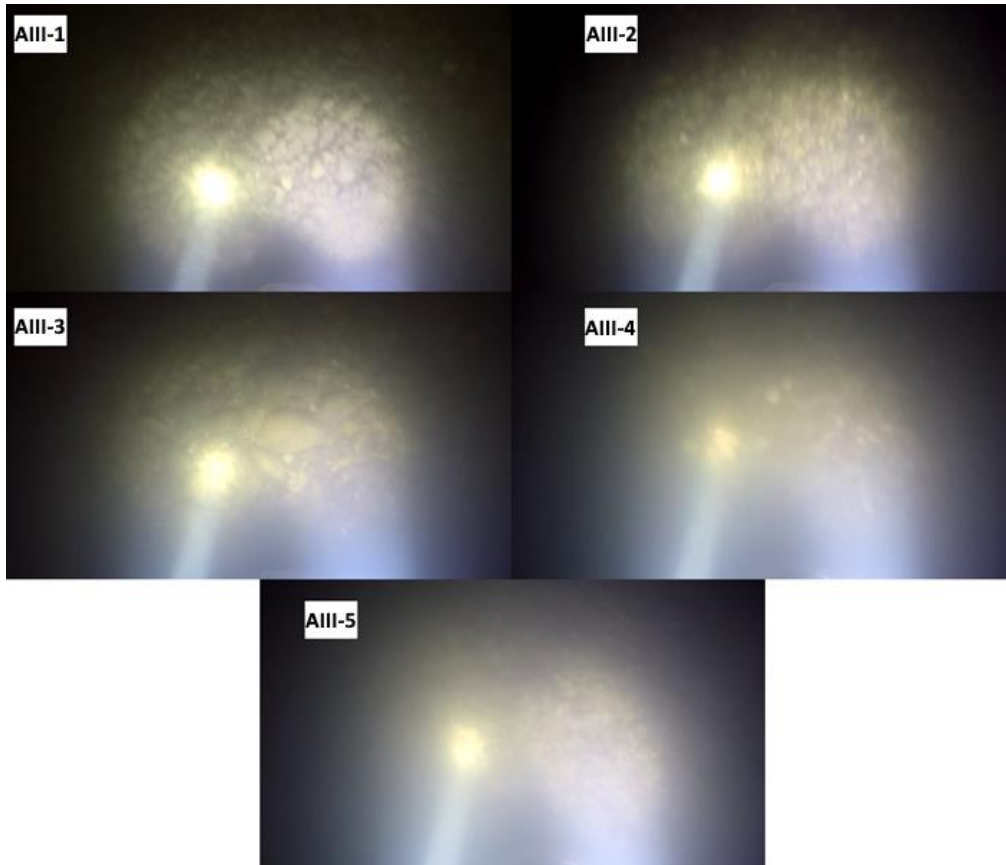


1116 Figure D2: Sediment fraction percentages in Section A - III, recognised by the AI. The visual evaluation included three
 1117 classes: gravel – G, sandy gravel – sG, gravelly sand - gS). The fractions of the physical samples are shown as verticals.
 1118



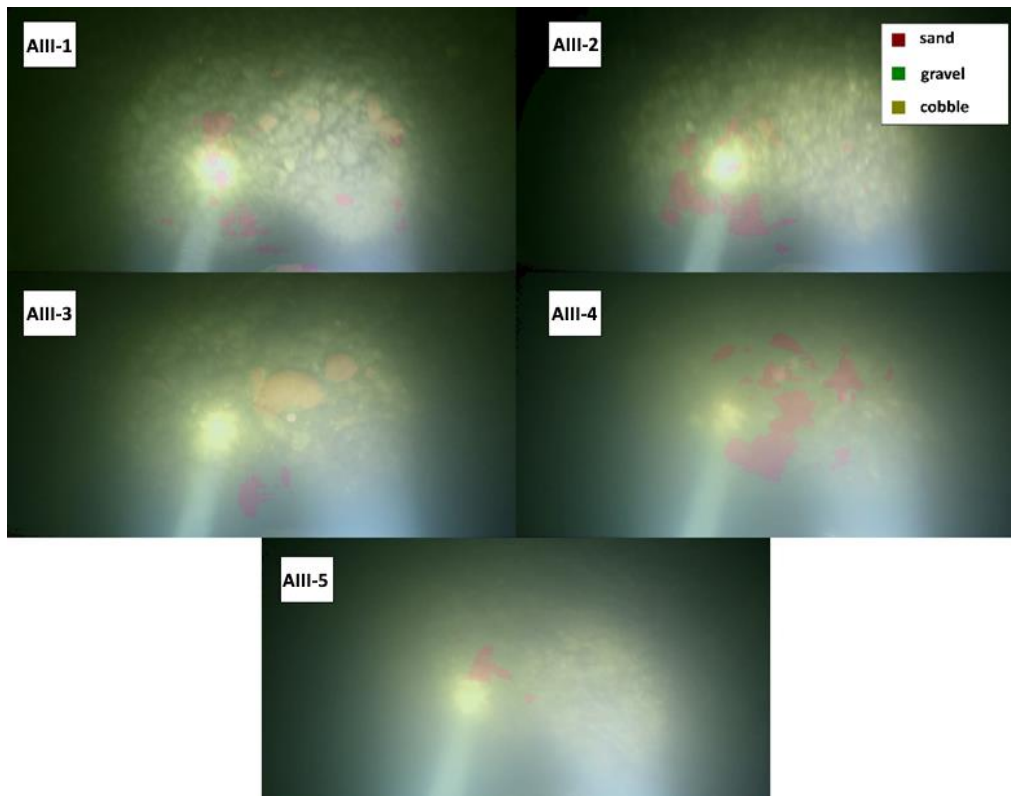
1119
1120
1121

Figure D3: Comparison of sediment fraction % at the sampling locations from the moving-averaged DL detection, conventional sieving and the wavelet-based image processing method. Section A - III.



1122
1123 Figure D4: Riverbed video images at the sampling points in Section A - III.

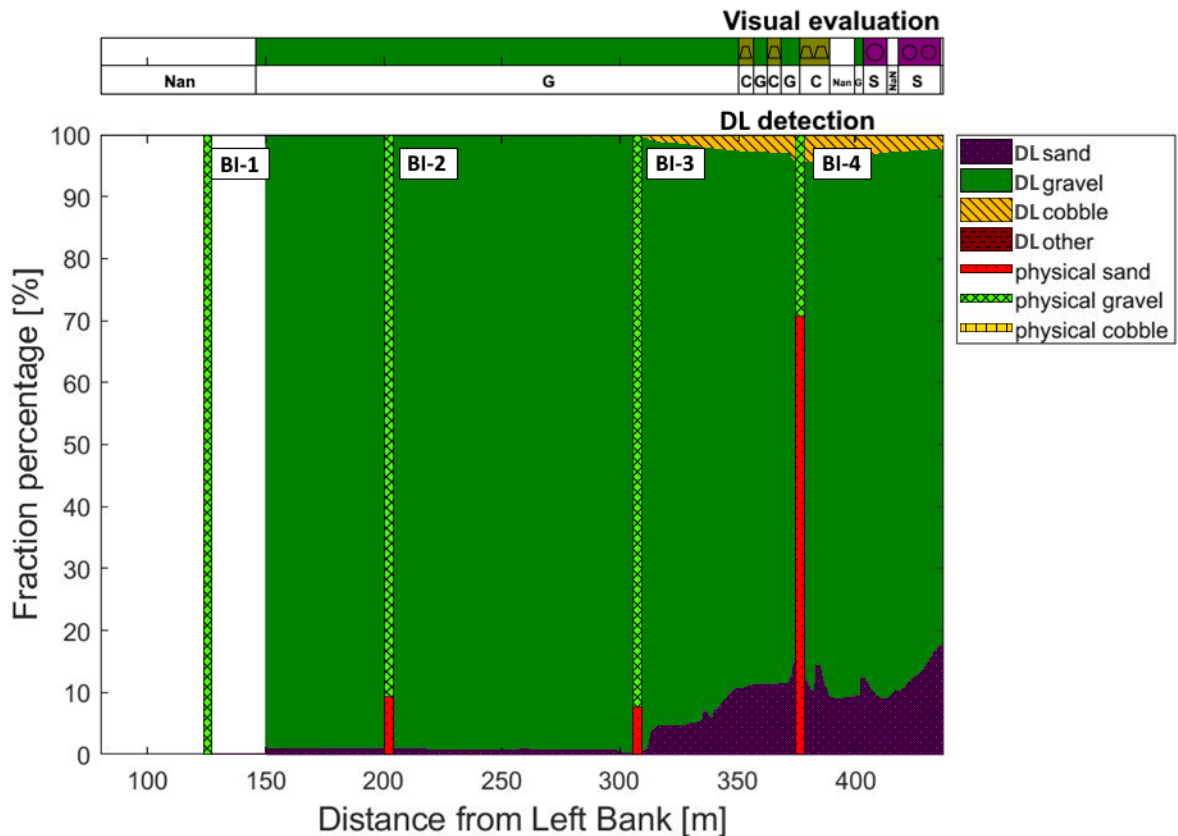
1124



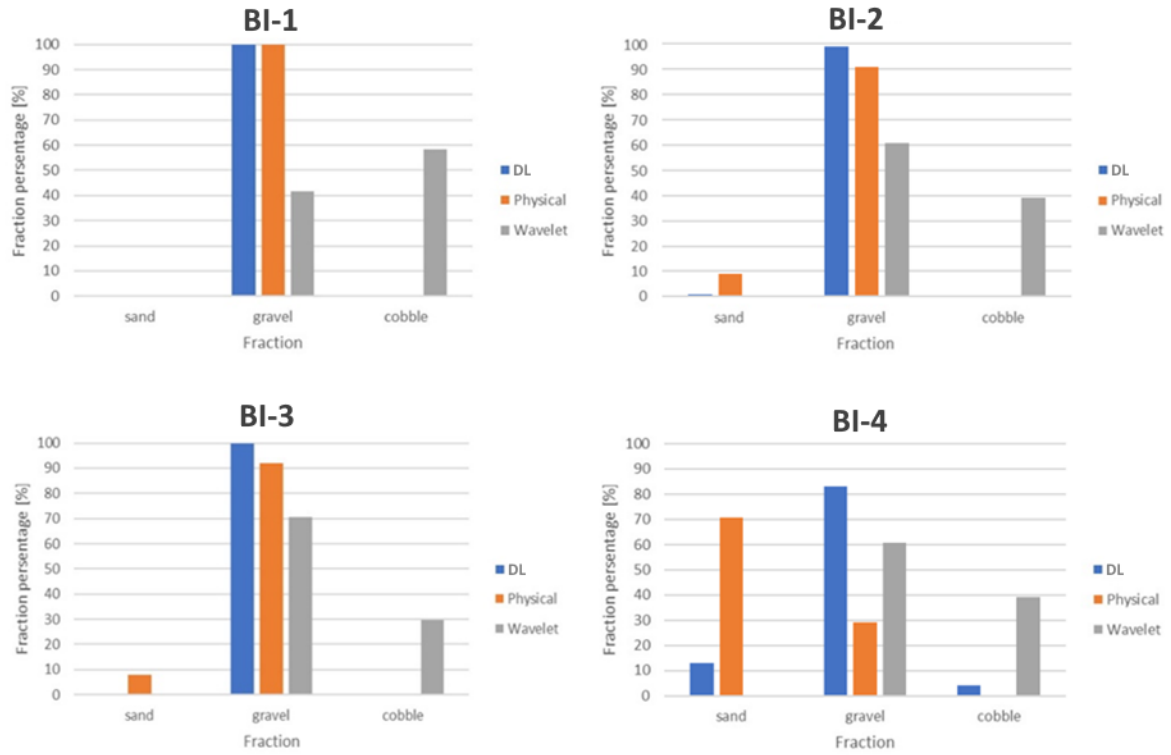
1125
1126 Figure D5: Riverbed video images overlapped with their raw, DL detection result, at the sampling points in Section A
1127 - III.
1128



1130
 1131 Figure E1: The path of the vessel and camera in Section B - I, Site B. The polyline is coloured based on the sediment
 1132 seen during visual evaluation of the video. Yellow markers are the locations of physical bed material samplings. (Map
 1133 created with Google Earth Pro)

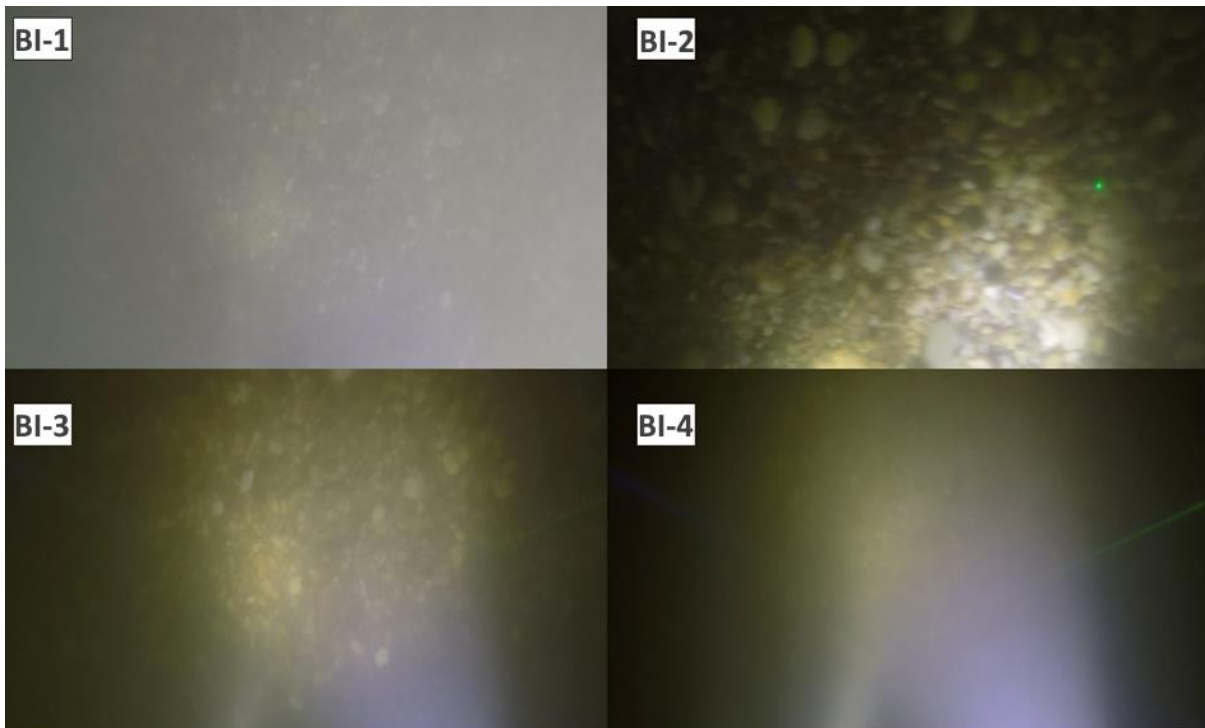


1134
 1135 Figure E2: Sediment fraction percentages in Section B - I, recognised by the AI. The visual evaluation included two
 1136 classes: gravel – G, sand – S). The fractions of the physical samples are shown as verticals.



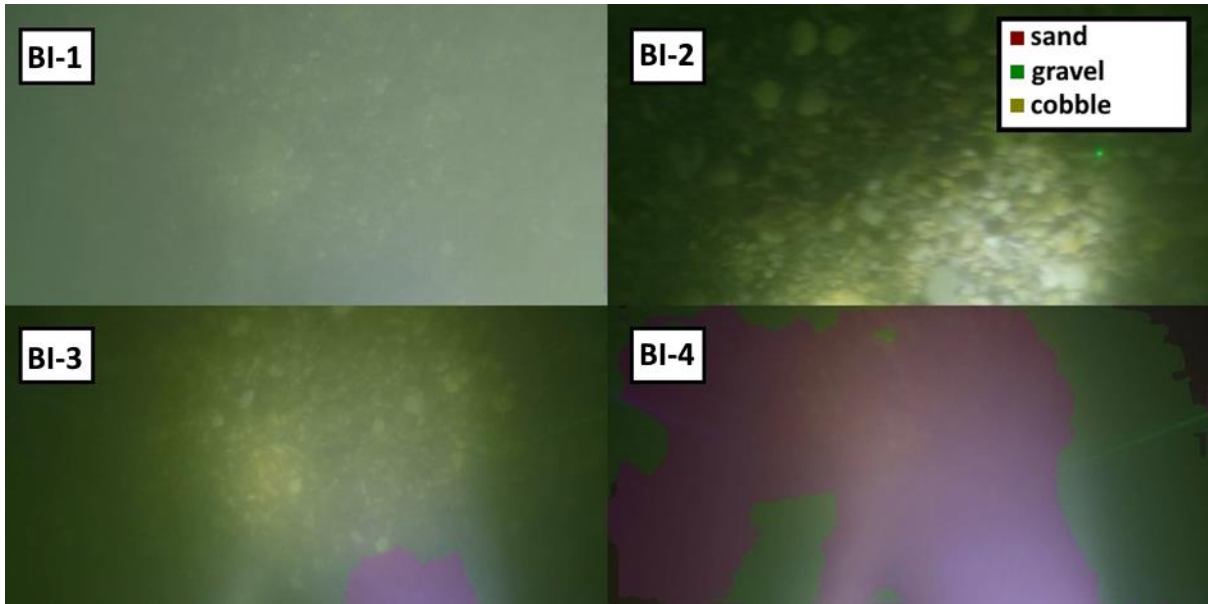
1137
1138
1139

Figure E3: Comparison of sediment fraction % at the sampling locations from the moving-averaged DL detection, conventional sieving and the wavelet-based image processing method. Section B - I.



1140
1141
1142

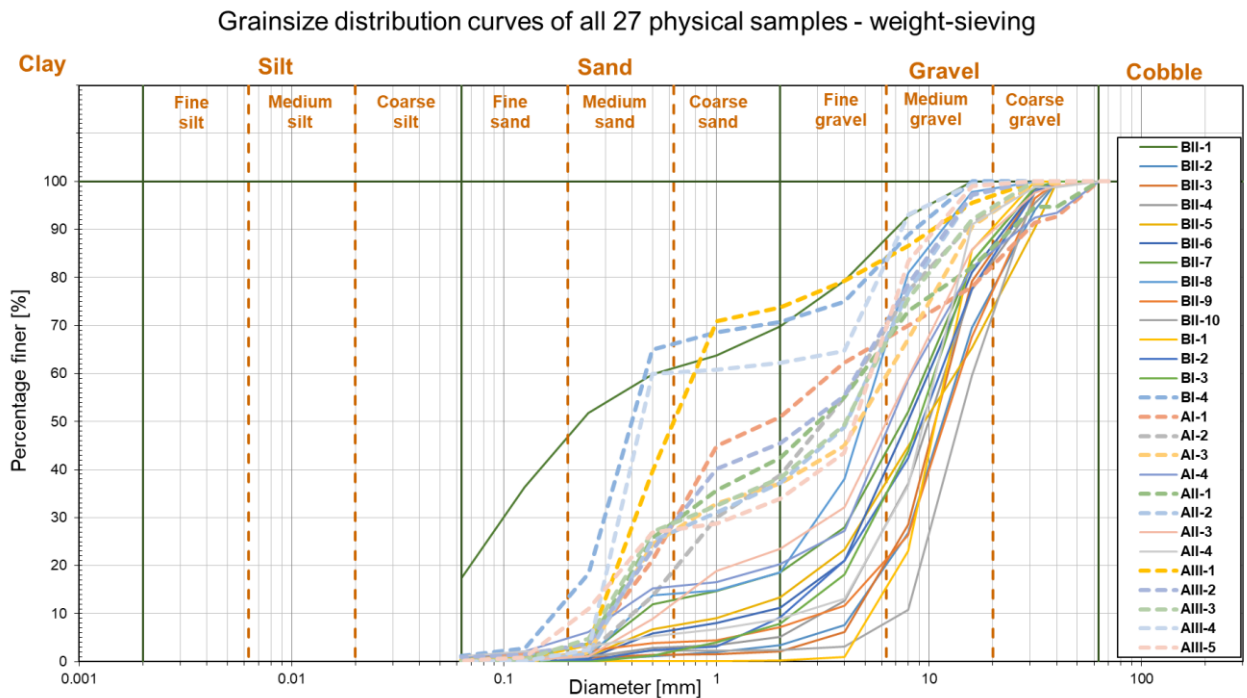
Figure E4: Riverbed video images at the sampling points in Section B - I.



1143
1144 Figure E5: Riverbed video images overlapped with their raw, DL detection result, at the sampling points in Section B
1145 - I.

1146

1147 Appendix F



1148
1149 Figure F1: Grainsize distribution curves of the 27 sieved physical samples. 11 curves categorised as Outlier Type-A are
1150 showcased with dashed lines. The shapes of these curves are representing bimodal (gap graded) sediment distributions,
1151 which typically refers to bed armouring (i.e., excess of a certain particle size, a coarser surface layer protects a finer
1152 subsurface layer from being washed away). Hence, analysing images of the surface layer could not represent these
1153 complex distributions inherently.